

Stellar Disc Truncations and Extended Haloes in Face-on Spiral Galaxies

S. P. C. Peters¹, P. C. van der Kruit^{1*}, J. H. Knapen^{2,3}, I. Trujillo^{2,3}, J. Fliri^{2,3},
M. Cisternas², L. S. Kelvin^{2,3,4}

¹*Kapteyn Astronomical Institute, University of Groningen, P.O.Box 800, 9700AV Groningen, the Netherlands*

²*Instituto de Astrofísica de Canarias, VILCÁCTEA, E-38205 La Laguna, Tenerife, Spain*

³*Departamento de Astrofísica, Universidad de La Laguna, E-38205 La Laguna, Tenerife, Spain*

⁴*Institut für Astro- und Teilchenphysik, Universität Innsbruck, Technikerstraße 25' 6020 Innsbruck, Austria*

Accepted 2015 month xx. Received 2015 Month xx; in original form 2015 Month xx

ABSTRACT

We use data from the IAC Stripe82 Legacy Project to study the surface photometry of 22 nearby, face-on to moderately inclined spiral galaxies. The reprocessed and combined Stripe 82 g' , r' and i' images allow us to probe the galaxy down to 29-30 r' -magnitudes/arcsec² and thus reach into the very faint outskirts of the galaxies. Truncations are found in three galaxies. An additional 15 galaxies are found to have an apparent extended stellar halo. Simulations show that the scattering of light from the inner galaxy by the Point Spread Function (PSF) can produce faint structures resembling haloes, but this effect is insufficient to fully explain the observed haloes. The presence of these haloes and of truncations is mutually exclusive, and we argue that the presence of a stellar halo and/or light scattered by the PSF can hide truncations. Furthermore, we find that the onset of the stellar halo and the truncations scales tightly with galaxy size. Interestingly, the fraction of light does not correlate with dynamic mass. Nineteen galaxies are found to have breaks in their profiles, the radius of which also correlates with galaxy size.

Key words: galaxies: photometry, galaxies: spiral, galaxies: structure

1 INTRODUCTION

Truncations in edge-on stellar discs were first discovered by van der Kruit (1979), who noted that the radial extent of these galaxies did not grow with deeper photographic exposures, in contrast with the vertical extent. Truncations are very sharp, with scalelengths of less than 1 kpc and typically occur at around four to five times the exponential scalelength of the inner disc (van der Kruit & Searle 1981a,b, 1982; Fry et al. 1999; de Jong et al. 2007; Barteldrees & Dettmar 1994; Kregel et al. 2002). In a recent extensive analysis of 70 edge-on galaxies in the near-IR, taken from the *Spitzer Survey of Stellar Structure in Galaxies* (S⁴G), Comerón et al. (2012) concluded that about three out of four thin discs are truncated.

While truncations in edge-on galaxies have been observed for the last 35 years, their face-on counterparts remain elusive. This is in part due to shorter line-of-sight in-

tegration through face-on and moderately inclined galaxies. Due to this, the expected surface brightness at four scalelengths is about 26 B -mag arcsec², only a few percent of the dark sky (van der Kruit & Searle 1981a, 1982). In recent times, various studies on inclined or face-on samples have been performed looking for such truncations. For comparison with the van der Kruit & Searle systems one would first concentrate on non-barred late-type systems. Pohlen & Trujillo (2006) studied such a sample of 90 moderately inclined, late-type systems through ellipse-fitting of isophotes in Sloan Digital Sky Survey (SDSS) data. They identified galaxies with truncations, but they also found cases where the discs continued as unbroken exponentials, or even showed an upturn in the outer parts. This latter behaviour was earlier found in barred early-type galaxies by Erwin et al. (2005), followed up by Erwin et al. (2008) on 66 barred and by Gutiérrez et al. (2011) on 47 unbarred, early-type galaxies. These studies led to a classification system, in which Type I designated exponentials out to the noise level, Type II with a turndown of the profile before that and Type III with an upturn.

* For more information, please contact P.C. van der Kruit by email at vdkruit@astro.rug.nl.

Pohlen & Trujillo (2006) found that 60% of their galaxies had a break in the profile between 1.5-4.5 times the scale-length followed by a steeper downbending. In 26 of their galaxies they included in their classification (in addition to the class Type II) a designation CT for ‘classical truncation’. These, they proposed were similar features as the truncations in edge-on systems.

This result has been disputed by van der Kruit (2008), who argued that these are in fact breaks similar to those found by Freeman (1970). Originally, van der Kruit & Searle (1981a, 1982) had found that the truncation in edge-on systems occurred at 4.2 ± 0.5 scale lengths, while Kregel & van der Kruit (2004) quoted 3.6 ± 0.6 scale lengths. In the latter paper it was estimated that this corresponded to a face-on surface brightness at the onset of the truncations of 25.3 ± 0.6 R-mag arcsec⁻². In contrast the radii of the features in the Pohlen & Trujillo (2006) study were at 2.5 ± 0.6 scale lengths and surface brightness 23 to 25 in r' (see their Figure 9). The view of breaks and truncations as two separate features was proposed also by Martín-Navarro et al. (2012). In a study of 34 edge-on spiral galaxies, they found that the innermost break occurs at $\sim 8 \pm 1$ kpc and truncations at $\sim 14 \pm 2$ kpc in galaxies.

Another reason for the elusiveness of face-on truncations is the lopsided nature of spiral galaxies at faint levels. This is clearly demonstrated by the $m = 1$ Fourier component of surface brightness maps (Rix & Zaritsky 1995; Zaritsky & Rix 1997; Zaritsky et al. 2013) and in polar projected contour maps (Pohlen et al. 2002). In face-on galaxies like NGC 628 an isophotal map shows that the outer contours have a much smaller spacing than the inner ones (Shostak & van der Kruit 1984; van der Kruit 1988). Due to the lopsided nature of these galaxies, the typical method of fitting ellipses to the profile will smooth out the truncations. Peters et al. (2017) devised two alternative methods to derive the profiles. Although the techniques looked promising, they were hampered by the limited sky brightness of the SDSS images and did not detect any truncations.

A third reason may be that at the expected surface brightness levels in face-on galaxies, truncations will be of similar brightness as stellar haloes. In Λ CDM cosmology, galaxies build up hierarchically, with small objects merging together under their mutual gravity to form ever larger objects, leading up to the structures we see today (White & Rees 1978). The lopsided outer edges of spiral galaxies are caused by tidal interactions and in-fall from these structures. Stellar haloes are remnants of this merger process, a graveyard of long-gone galaxies. Faint stellar haloes have been successfully detected around spiral galaxies. This is often done by resolving the individual stars, using very deep observations, for example as those obtained using the Isaac Newton Telescope by Ferguson et al. (2002), or the Hubble Space Telescope by Monachesi et al. (2013). Using surface photometry, Bakos & Trujillo (2012) found that at very faint levels the radial profiles of seven disc galaxies indicate the presence of a stellar halo at levels of 29 to 30 r -mag/arcsec², but found no evidence for truncations. They argue that these haloes may be the cause of the hidden truncations in the radial profiles of face-on galaxies. Recently, Martín-Navarro et al. (2014) used a theoretical model to demonstrate that a stellar halo can indeed outshine truncations in a face-on galaxy.

In this context it is relevant to consider the up-bending profiles, designated Type III. As noted above this behaviour was first found by Erwin et al. (2005); Pohlen & Trujillo (2006) found this in 30% of their galaxies. In the latter paper a prominent example of this was NGC 3310, which is a well-known case of an outer disturbance. In this system it is in the form of a ‘bow and arrow’, which would be the cause of the upbending profile. NGC 3310 has been studied in detail by e.g. van der Kruit (1976) and Kregel & Sancisi (2001) and is a clear case of a merger. This led van der Kruit & Freeman (2011) to examine deep SDSS images of the Type III galaxies in Pohlen & Trujillo (2006), which indicated that many, if not all, of these show signs of interaction or distortion at faint levels.

The presence of Type III profiles has been established in galaxy samples covering a wide range of Hubble types and environments (Roediger et al. 2012; Herrmann et al. 2013; Laine et al. 2014). These may represent outer disc structures not related to merging and that are intrinsic to the disc structure. To ensure that we do not include any distorted outer discs, we have in the present study concentrated on undisturbed systems, selected on deep SDSS images, and such systems would be excluded.

The aim of this paper is to detect truncations and stellar haloes in surface photometry using data for a sample of face-on and inclined spiral galaxies available in the new IAC Stripe 82 Legacy Project (Fliri & Trujillo 2016, in preparation). This project is a careful reprocessing of the SDSS Stripe 82 data, improving over the regular SDSS data by ~ 2 magnitudes. This allows us to trace the profiles down to ~ 30 r -mag/arcsec², a depth which few studies have reached before (e.g. Zibetti & Ferguson 2004; Zibetti et al. 2004; Jablonka et al. 2010; Bakos & Trujillo 2012; Trujillo & Bakos 2013). We use four different photometric techniques to analyse the data, the classical ellipse fitting routines, the Principle Axis Summation (PAS) and Equivalent Profiles (EP) from Peters et al. (2017) and a new technique that we call Rectified Polar Profiles, introduced here. We find that using these techniques, we can indeed identify both stellar haloes and truncations in galaxies.

The remainder of this paper has the following outline. In Section 2 we describe the sample and the data reduction. Section 3 introduces the various photometric techniques we used. The results are presented in Section 4, followed by a discussion in Section 5. We summarize the results in Section 5.6. The results for the individual galaxies are presented in the online Appendix.

2 GALAXY SAMPLE

2.1 Sample Selection

The goal of our project is to derive stable, extremely deep surface photometry of face-on to moderately inclined disc galaxies. Our initial sample consisted of all galaxies in the SDSS Stripe 82 sample with a diameter larger than one arcminute. This set consists of 177 elliptical, irregular, face-on and edge-on disc galaxies.

The SDSS jpeg colour images for each galaxy were

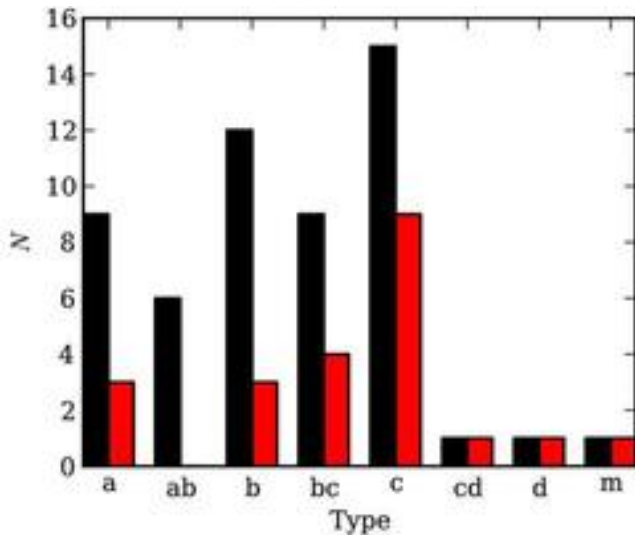


Figure 1. Histogram of the distribution of Hubble types for the sample of disc galaxies. The left black bars shows the distribution for the 54 initial disc galaxies that were retrieved. The right red bars show the distribution of the final 22 galaxies used in our analysis. Classification based on the primary listing in NED.

downloaded using the Finding Chart Tool¹. Each image was visually inspected for type, possible signs of distortions, mergers and nearby objects, which might cause problems with the photometry. We accepted those face-on to moderately inclined disc galaxies for which we found no potential issues. The criterion was then a judgement that the discs were visible sufficiently well to derive radial profiles. In total these were 54 galaxies. These galaxies were then retrieved from the IAC Stripe 82 Legacy Project pipeline. The images were again visually inspected for any form of distortion, nearby objects and possible issues of the sky-levels. This left us with a final sample of 22 galaxies, for which we are confident of the extracted surface photometry down to 29-30 r' -mag/arcsec². The primary properties of this sample are shown in Table 1. We show the distribution of Hubble types in Figure 1.

2.2 Image Reduction and Calibration

The IAC Stripe 82 Legacy Project (Fliri & Trujillo 2016) produces (co-)adds of the whole Stripe 82 data set using an automated (co-)addition pipeline. The pipeline queries all available data from the SDSS archive, aligns them photometrically and calibrates them to a common zero-point using calibration tables provided by SDSS for each image. Accurate values of the sky background are determined on object-masked images and subtracted from the calibrated images. Images with large sky backgrounds, notable sky gradients, large PSF widths and images affected by clouds or taken under bad transparency conditions are removed from the final stack. Finally, all images passing the selection criteria are re-gridded onto a field of view of 0.25 square degrees and median-combined by SWarp (Bertin

et al. 2002). The IAC Stripe 82 Legacy Project is presented at www.iac.es/proyecto/stripe82. The (co-)added images produced for this project are considerably smaller in size than in the data release (100 compared to 900 square arcminutes), and the images have been centred on each of the target galaxies to facilitate profile extraction.

The (co-)added images are calibrated to a zero-point $aa = -24$ mag, and are already corrected for airmass and extinction. With an area $dS = 0.396'' \times 0.396''$ of each pixel in SDSS and an exposure time of 53.907456 s, the conversion from counts to magnitudes can be performed by using Equation 2:

$$\mu_0 = aa + 2.5 \log_{10}(\text{exptime} \times dS), \quad (1)$$

$$\text{mag} = -2.5 \log_{10}(\text{counts}) + \mu_0. \quad (2)$$

Since the mosaicking process leaves the various bands at exactly the same pixel position, combining the g' , r' and i' images is simply a matter of taking the average of the three. We do this to increase the signal-to-noise ratio and thus to extend our analysis further out in the galaxies. Combining the three bands is destructive to the zero-point calibration process and we thus need to re-calibrate the data. We measure ellipse profiles on both the original r' and new combined images. We find the new calibration zero-point μ_0 of the (co-)added profiles by shifting the profiles up or down, until they align with the calibrated r' -band profiles.

2.3 Object Masking and Background Treatment

Any study of surface photometry requires a careful removal of background and foreground objects. At the 29-30 r' -mag/arcsec² depth we aim to reach in the case of the IAC Stripe 82 Legacy Project, bright stars far outside the frame can still contribute flux. We therefore need to model and remove this contamination.

As a first step, a smoothed and stacked version of the various bands was inspected and object masks were defined by hand. By repeating this process multiple times, we were able to remove all faint background sources from the image. At this stage, an elliptical mask was defined for which we were certain that it comfortably covered the entire galaxy. The remaining background was then modelled using the following method. Around each pixel that was not part of an object mask and not in the galaxy mask, a 21×21 pixel ($\sim 8.3'' \times 8.3''$) box was defined, from which we selected a sample of all pixels not part of any mask. A sigma-clip of 2.5σ was run over this sample, after which the background value was measured as the median of the remaining pixels. By repeating this process for each pixel, a map of the large-scale structure in the background was created. In this background model, we then selected a 50 pixel wide ring around each galaxy mask, to which we fit a 2D linear plane. This plane was extrapolated to model the background inside the galaxy mask. The complete background model was subsequently subtracted from the original image. We demonstrate the background subtraction process in Figure 2.

Our next step was to measure the uncertainty and noise in the background. This was done on the original combined data, using the same mask as the one used in the background-modelling step. There were always over 200,000 pixels used in the measurement. We use the Python package

¹ The URL is cas.sdss.org/dr7/en/tools/chart/chart.asp.

Galaxy	Type	M_b	M_B	v_{rad} [km/s]	D [Mpc]	i [°]	V_{rot} [km/s]	PA [θ]
IC 1515	Sb	14.4	-20.5	6560	93.1	26.8	332.6	252.3
IC 1516	Sbc	14.2	-21.0	7170	101.7	17.6	418.7	202.1
NGC 450	SABc	12.8	-19.3	1729	24.5	45.5	146.4	171.6
NGC 493	Sc	13	-19.7	2277	32.3	72.9	158.2	148.9
NGC 497	SBbc	13.8	-21.6	7932	112.5	65.4	302.9	219.5
NGC 799	SBa	14.2	-20.5	5730	81.3	28.9	341.8	159.1
NGC 856	Sa	14.2	-20.5	5786	82.1	38	284.2	113.6
NGC 941	SABc	13	-18.8	1557	22.1	44.7	123.0	254.1
NGC 1090	Sbc	12.6	-20.4	2660	37.7	64.4	188.2	190.6
NGC 7398	Sa	14.8	-19.6	4735	67.2	48.4	235.4	163.1
UGC 139	SABc	14.5	-19.3	3899	55.3	64.6	172.7	170.6
UGC 272	SABc	15.2	-18.5	3821	54.2	67.2	133.8	219.0
UGC 651	Sc	16.1	-18.4	5064	71.8	68.9		256.3
UGC 866	Sd	15.6	-16.5	1710	24.3	71.2	80.3	146.9
UGC 1934	Sbc	15.5	-20.8	11996	170.2	74.7	297.5	200.4
UGC 2081	SABc	15	-17.8	2522	35.8	54.7	122.0	163.1
UGC 2311	Sb	14.1	-21.1	6901	97.9	30.9	343.0	170.2
UGC 2319	Sc	15.5	-19.7	6827	96.8	72.8	202.6	45.5
UGC 2418	SABb	15.1	-20.2	6671	94.6	46.7	205.4	184.5
UGC 12183	Sbc	15.5	-19.0	4728	67.1	54.8	164.6	120.4
UGC 12208	Scd	15.2	-18.7	3342	47.4	42.8		156.2
UGC 12709	SABm	14.4	-18.6	2700	38.3	51.8	103.7	229.7

Table 1. Sample properties. Morphological type, apparent magnitude M_b , absolute magnitude M_B (both in B -band), radial velocity v_{rad} and maximum rotational velocity V_{rot} from HYPERLEda, based on width at 20 of the HI flux and corrected based on the inclination from this work (Paturel et al. 2003; Springob et al. 2005; Theureau et al. 1998; Meyer et al. 2004). Distance D from NED, based on Virgo + GA + Shapley and assuming H_0 70.5 km/sec-Mpc, Ω_{matter} 0.27 and Ω_{vacuum} 0.73. The absolute magnitude has been distance corrected using this distance and has been corrected for foreground extinction based on Schlafly & Finkbeiner (2011). Inclination i this work. No rotational velocities are available in the literature for UGC 651 and UGC 12208. Position Angle PA based on this work.

SCIPY.STATS.BAYES.MVS to perform a Bayesian estimation of the confidence in the mean and the standard deviation (Oliphant 2006). The uncertainty is based on the average confidence limit for the mean. The pixel-to-pixel noise is taken as the standard deviation of the sample. This is indicated in the figures in the online appendix.

3 PROFILE EXTRACTION

In this section we discuss our four methods to extract radial surface brightness profiles from the observed distributions. The first three have been used before, but the fourth one is new.

3.1 Ellipse Fitting

We use the IRAF package *stsdas.ellipse* (Jedrzejewski 1987; Busko 1996) to extract ellipse profiles from the data. In a first pass, the package was allowed to run with the position angle and inclination as free parameters. This was done to get the best estimates for the various parameters. We use the innermost ellipse for the exact position of the center of the galaxy. The position angle and inclination were measured from the 25th magnitude ellipse, where we define the inclination as $i = \arccos(b/a)$, using major and minor axis a and b . This also gives us the ellipticity e . In the second pass, the central position, position angle and inclination were fixed and the method was run again to produce the final radial profiles.

3.2 Equivalent Profiles

The original method for deriving the photometry of galaxies was the use of the Equivalent Profiles method EP (de Vaucouleurs 1948). The modern-day version of the EP was introduced by Peters et al. (2017), in an attempt to understand the reliability of the ellipse fitting. Compared to the latter, EP works in a fundamentally different way. Rather than taking a radius R and measuring a corresponding average surface brightness $\mu(R)$, this method works in the opposite direction. Starting with the lowest magnitude in the image and working up from there, for each magnitude it counts the number of pixels N that are equal to or brighter than the current magnitude. We make the reasonable assumption that the galaxy forms an ellipse on the sky, with a shape based on the 25th magnitude parameters from the ellipse fitting in Section 3.1. Since each pixel covers a small surface on the sky of $0.396'' \times 0.396''$, we can use the total amount of pixels N belonging to brightness μ to estimate a total surface S and from there use the ellipse to estimate an equivalent (major axis) radius R .

Peters et al. (2017) extensively tested the technique on a sub-sample of 29 galaxies defined previously by Pohlen & Trujillo (2006), and found that the results produced by EP and ellipse fitting are remarkably similar. At magnitudes near the pixel-to-pixel noise, EP tends to go wrong as it includes noise peaks into the equivalent radius. Peters et al. (2017) set out to include adaptive smoothing and masking of the background to avoid this problem, but overall the method was found to work reliably only above the pixel-to-pixel noise limit.

In this work, we rotate and centre the original image,

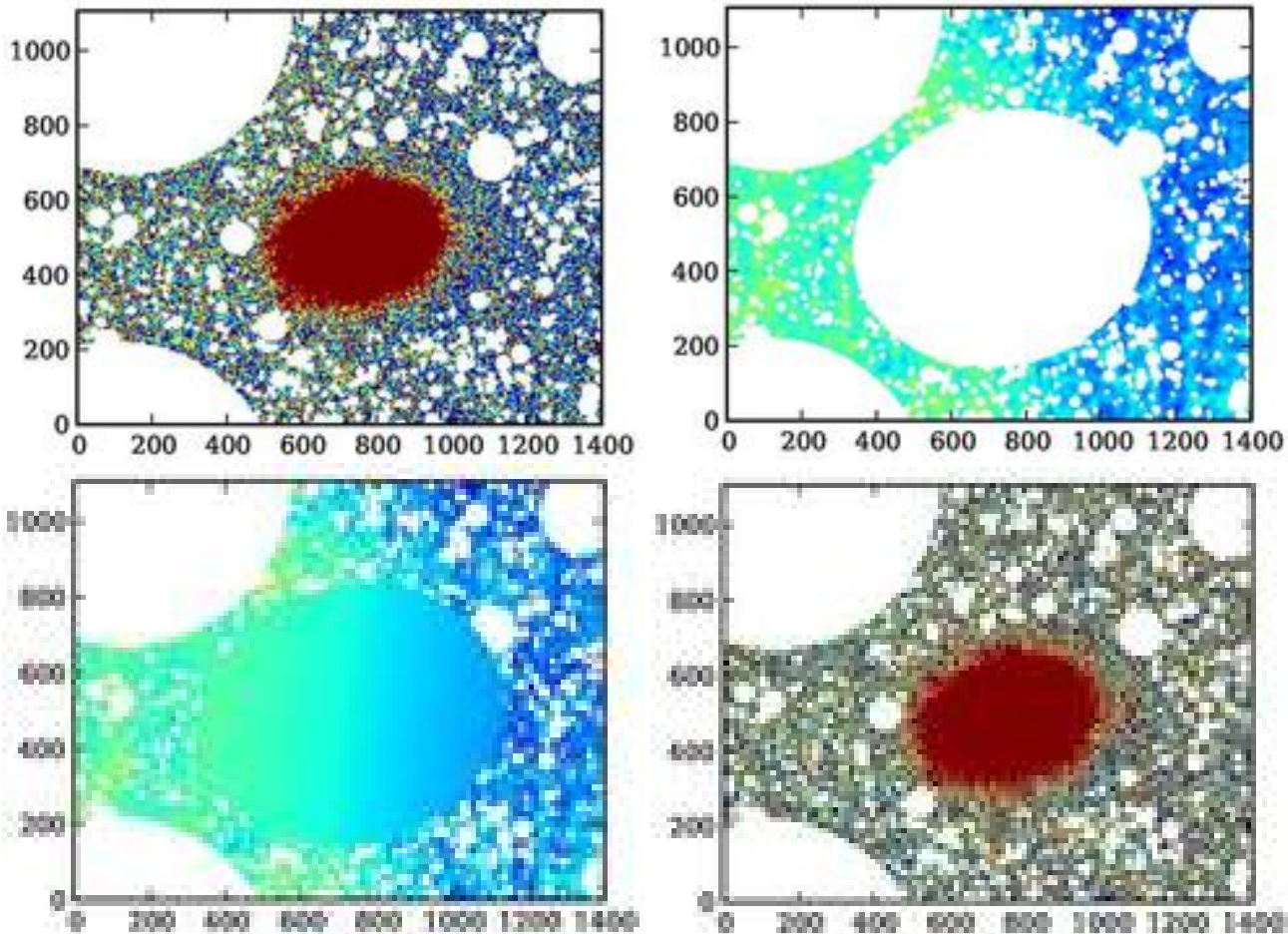


Figure 2. Overview of the background modelling process for the galaxy NGC 941. Top left: the original image with objects masked. Top right: the model created for the sky, excluding the galaxy. Lower left: the sky model including the galaxy. Lower right: the final image with the sky model subtracted from the observation. In all figures, the colour scales run from -1.0 to 1.0 ADU. Horizontal and vertical axes are in pixels (one pixel = $0.396''$). North is right, east is top.

based on the positioning as measured using the ellipse profiles in Section 3.1. We define an elliptical mask with a trust radius R_{trust} set by eye, beyond which the data are set to blank. Similar to Peters et al. (2017), we again plot our profiles out to the radius where over- or under-subtracting the data by two times the uncertainty leads to a deviation of more than 0.2 magnitudes, compared to the original profile.

3.3 Principle Axis Summation

In an attempt to recognize the truncations seen in edge-on galaxies with respect to face-on galaxies better, Peters et al. (2017) developed the Principle Axis Summation method PAS. The PAS has been developed to project face-on galaxies into edge-on galaxies, in the hope that features similar to truncations appear. While the method itself was successful, true truncations remained elusive, due to the much shallower nature of the original SDSS data (Peters et al. 2017).

Similar to the EP, we again rotate and centre the image, after which we apply the same elliptical blanking mask at trust radius R_{trust} . The PAS then partitions the galaxy into four quadrants. Quadrants with visible problems, for example a foreground star, were removed. Each quadrant

is then summed onto the major axis, after which the main profile is formed by the median of the accepted quadrants. A dynamic binning algorithm is applied to ensure that the profile has a signal-to-noise ratio of at least two.

The uncertainty in each point is different, due to the varying number of pixels involved in the sum. Similar to Peters et al. (2017), for each point, we repeat the PAS technique many times on randomly drawn samples from the set of background pixels defined in Section 2.3, which gives a good estimate of the uncertainty.

To demonstrate the effect of PAS and the way we expect truncations to appear in face-on galaxies, we have applied the method to the edge-on galaxy UGC 2584, for which the data are also available in the IAC Stripe 82 Legacy Project, and which we have reduced in the exact same ways as the face-on galaxies in this sample. The PAS results are shown as the red (top) curve in Figure 3, whereas the blue (lower) curve demonstrates the surface brightness measured along the central plane of the galaxy. It is clear that a truncation is visible at a radius of 15 kpc, evident from both methods.

As noted in Peters et al. (2017), the PAS profiles have units of magnitudes/arcsec, as the minor axis summation can reach higher values in nearby galaxy with large appar-

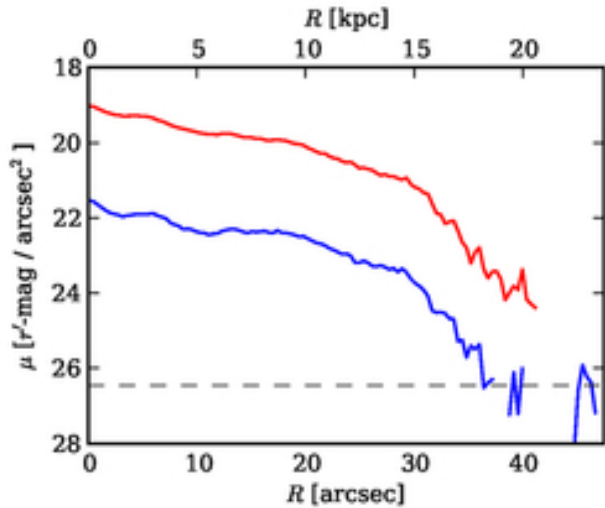


Figure 3. A truncation in the edge-on galaxy UGC 2584. The lower, blue curve shows the r' -band surface brightness measured in a strip along the central plane of the galaxy. The top, red curve shows the PAS profile for this galaxy in arbitrary units. As can be seen clearly from the figure, the truncation is visible in both methods, starting at $R \simeq 30''$ and 15 kpc. The dashed, gray line represent the pixel-to-pixel noise.

Galaxy	x1	x2	x3	x4	x5	x6	r_{trust}
IC 1515	11.1	14.5	16.7	25.6	30.0	44.5	44.5
IC 1516	24.8	43.1	44.2	53.9			99.3
NGC 450	3.9	9.0	9.7	14.2	15.5	18.1	18.3
NGC 493	6.3	12.6	13.9	22.7	27.1	41.7	42.5
NGC 497	12.6	20.1	26.4	50.3	67.9	88.0	90.6
NGC 799	8.1	17.1	21.3	31.6	37.6	47.0	48.7
NGC 856	10.5	41.9					41.9
NGC 941	4.0	7.3	8.9	14.5			29.0
NGC 1090	21.2	26.8	29.0	39.1			46.0
NGC 7398	6.0	8.0	10.0	17.9	21.9	39.8	39.8
UGC 139	10.7	16.6	19.5	24.4	26.3	45.8	45.8
UGC 272	2.7	6.4	10.1	15.6	18.3	30.2	30.2
UGC 651	3.2	8.6	9.7	15.0	16.1	25.8	25.8
UGC 866	2.8	6.9	7.9	9.8			13.1
UGC 1934	20.7	31.0	31.0	33.0	54.7	86.7	91.8
UGC 2081	5.0	11.6	13.2	19.0			19.0
UGC 2311	10.4	14.5	17.6	27.0	29.0	33.2	46.7
UGC 2319	2.9	8.8	10.8	22.5	24.5	32.3	40.2
UGC 2418	2.9	8.8	11.8	27.4	28.4	31.9	44.1
UGC 12183	1.2	4.6	5.8	13.8	15.0	28.8	32.6
UGC 12208	2.4	5.9	7.1	11.9	14.3	16.6	18.5
UGC 12709	4.8	10.9	13.3	18.2	19.4	24.2	25.7

Table 2. Fit regions in [kpc]

ent sizes. The result of this is that while the profile itself is reliable, its vertical offset and extent compared to the other profiles varies. For the sake of comparison, we therefore choose to fix the central brightness as seen from the PAS at one magnitude lower than the central brightness as measured from the ellipse profiles.

3.4 Rectified Polar Plots

One possible reason that truncations in face-on galaxies are in principle difficult to see is that galaxies do not remain circularly symmetric, but become ragged or lopsided towards the faint outskirts. Any method of analysis that involves azimuthal averaging or assumptions on azimuthal symmetry would smooth such features out, since no galaxy is perfectly symmetric van der Kruit & Freeman (2011). Pohlen et al. (2002) plotted the isophotes of the galaxy NGC 5923 in polar coordinates (their Figure 9), which illustrates this. These authors demonstrated that taking individual sliced rows in this polar plot did not significantly impact the inner slope or blur the outer slope. We feel however that at the very faint outskirts of galaxies as we are studying this effect may still be significant.

Here, we will continue and expand upon the work by Pohlen et al. (2002). First, we project all galaxies into polar coordinates. We note that the outskirts of most galaxies indeed suffer from irregularities, which would smooth out possible truncations in any ellipse-averaging scheme.

We therefore attempt to ‘rectify’ the polar plots (RPP), such that the outer radii become well behaved. A boxcar smoothing was applied to the data, such that in the azimuthal direction the data are smoothed by a window of length 15° , one centered on one side of the major axis and then moving arounds the galaxy. In the radial direction the smoothing is effectively the same as the pixel size, so no radial details would be lost. We define various target brightness levels for rectification, specifically we tried every half magnitude between 25 and 27 r' -mag/arcsec². Along each radial sector-profile, we measure the first crossing of this rectification target brightness. The median over all azimuths of this first crossing radius yields a target rectification radius. Each sector of fixed azimuth in the original image is then stretched or compressed, such that the radius of the first crossing as seen in the smoothed image matches the target rectification radius.

The polar plot is partitioned into 12 azimuthal sectors in order to deal with problems in the image. In cases where the sector suffered from issues, for example due to masking, the entire sector was excluded from the analysis. The procedure has been illustrated for two galaxies, IC 1515 and UGC 12208 in Figure 4. The dark levels at larger radii shows that the noise illustrates the goodness of the fit for the background; the white areas result from the borders of the image and from bright stars that have been masked in the sky plot. The rectification has been performed here at 26 mag/arcsec², which corresponds to the yellow and light-green in the figure. Comparing the left- and right-hand panels (focus for example on the structure and curvature of the transition from the yellow to the orange coded levels) clearly shows the effects of the rectification at fainter levels. IC 1515 shows some lopsidedness at faint levels (larger extent in angles $\pm\pi$ at the left) that has been rectified in the process.

The final combined profiles are shown Figure 5 for the same two galaxies. Obviously only sectors that are not affected by difficulties such as background level or masked stars have been included. It shows PAS in red, the conventional ellipse fitting in blue, EP in green and RPP in purple, the latter for rectification target brightness levels of 25, 26 and 27 r' -mag/arcsec². Some offsets are applied as explained in

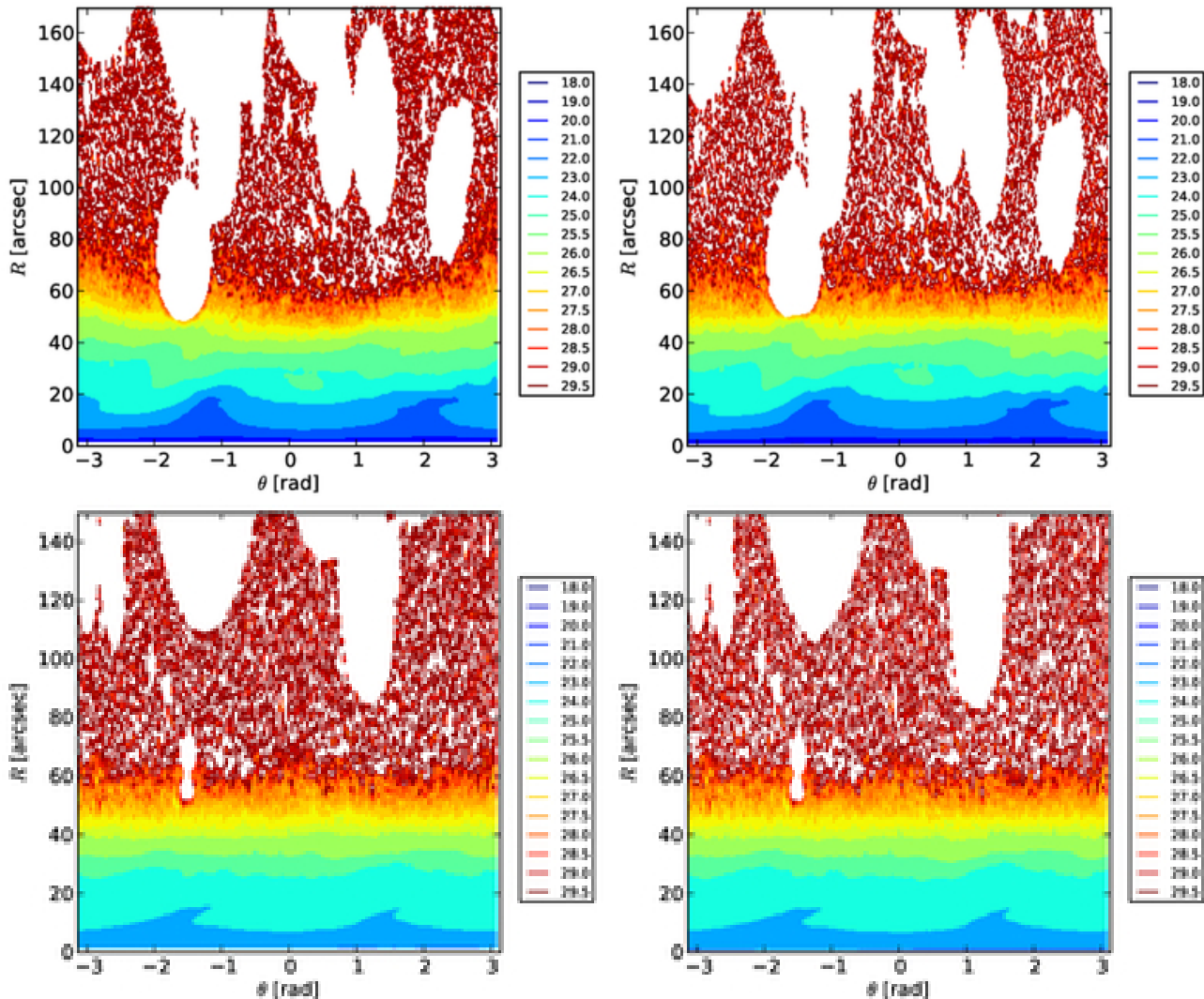


Figure 4. Polar plots for two of our galaxies, IC 1515 (upper) and UGC 12208 (lower). On the left the polar plot before rectification and on the right after rectification according to the procedure described in section 3.4 at a surface brightness of 26 mag/arcsec^2 . The minor axis is at position angles 0 and $\pm\pi$.

the caption. The dashed lines have been explained in the caption. We present a full set of illustrations for the full set of galaxies in our sample in the online appendix. In that appendix we show the RPP results only for 25, 26 and $27 r' \text{-mag/arcsec}^2$.

4 RESULTS

4.1 Measurement Strategy

Each set of profiles was inspected for the presence of breaks, truncations and haloes. We classified a feature as a break when there is a significant change in scale length inside and outside the radius of the feature. In almost every case the break can be associated directly with a feature in the galaxy, such as a bulge, bar or spiral arm. Breaks often occur in the inner, brighter parts of the galaxy, well above the pixel-to-pixel noise, and as such, they are visible in all four types of profiles. The rectified polar profiles are intended for de-

tecting truncations. We classified truncations of the profiles, when at levels fainter than $26 \text{ mag arcsec}^{-2}$ the profile definitely changes slope and drops towards the sky before disappearing in the noise. NGC 1090 has a break at $26.1 \text{ mag arcsec}^{-2}$, but has a very minor change in slope. We do not classify it as a truncation, but a break instead. Haloes are the opposite of truncations; when rather than steepening, the profile becomes less steep. Haloes should be visible in both the rectified polar profiles and in the ellipse profiles. As we expect truncations and haloes to occur at the outer edges of the profiles, deep below the pixel-to-pixel noise, the PAS and EP methods are not used.

To ensure unbiased results from the data, our team split up into groups. Each group went through all of the profiles and classified what they believed to be breaks, truncations and/or haloes. After that, we joined up again to discuss our findings and agree on any difficult cases.

We then set out to quantify our results by measuring the parameters of each feature. We defined fit-regions to the profile on both sides of a feature (shown in Table 2). In each

Galaxy	Break		Truncation		Halo		R_{25}
	R	μ	R	μ	R	μ	
IC 1515	$16.5^{+0.4}_{-0.4}$	$23.6^{+0.1}_{-0.1}$			$32.1^{+1.0}_{-1.3}$	$29.0^{+0.2}_{-0.3}$	21.3
IC 1516			$45.4^{+2.7}_{-4.9}$	$28.0^{+0.5}_{-0.8}$			27.5
NGC 450	$9.6^{+0.1}_{-0.1}$	$23.9^{+0.0}_{-0.0}$			$14.5^{+0.5}_{-0.6}$	$28.1^{+0.3}_{-0.4}$	11.1
NGC 493	$13.0^{+0.3}_{-0.4}$	$23.0^{+0.1}_{-0.1}$			$25.3^{+0.9}_{-0.9}$	$28.4^{+0.2}_{-0.2}$	17.9
NGC 497	$22.8^{+1.2}_{-1.3}$	$22.3^{+0.1}_{-0.1}$			$61.2^{+1.9}_{-2.0}$	$28.7^{+0.2}_{-0.2}$	40.9
NGC 799	$20.3^{+0.4}_{-0.5}$	$23.5^{+0.1}_{-0.1}$			$37.5^{+1.7}_{-3.1}$	$29.4^{+0.4}_{-0.7}$	24.9
NGC 856							21.1
NGC 941	$7.3^{+0.2}_{-0.2}$	$24.1^{+0.1}_{-0.1}$					8.9
NGC 1090	$26.1^{+0.2}_{-0.3}$	$26.1^{+0.2}_{-0.3}$					21.9
NGC 7398	$8.5^{+0.3}_{-0.4}$	$22.8^{+0.0}_{-0.0}$			$16.2^{+2.2}_{-1.6}$	$26.1^{+0.6}_{-0.5}$	15.3
UGC 139	$18.3^{+0.9}_{-1.4}$	$24.9^{+0.2}_{-0.2}$			$29.2^{+2.1}_{-2.6}$	$29.4^{+0.4}_{-0.7}$	19.1
UGC 272	$7.9^{+0.7}_{-1.0}$	$22.9^{+0.2}_{-0.2}$			$16.6^{+6.8}_{-4.8}$	$27.2^{+2.2}_{-1.9}$	13.3
UGC 651	$9.0^{+0.4}_{-0.6}$	$23.9^{+0.1}_{-0.2}$			$13.6^{+3.4}_{-1.9}$	$27.0^{+1.4}_{-0.9}$	11.6
UGC 866					$9.3^{+0.2}_{-0.2}$	$29.0^{+0.1}_{-0.1}$	5.1
UGC 1934	$25.8^{+1.7}_{-2.5}$	$23.5^{+0.3}_{-0.4}$			$40.9^{+1.3}_{-1.2}$	$26.6^{+0.1}_{-0.1}$	35.1
UGC 2081	$12.3^{+0.3}_{-0.3}$	$25.6^{+0.1}_{-0.1}$					10.6
UGC 2311	$17.4^{+0.3}_{-0.5}$	$23.8^{+0.1}_{-0.1}$			$32.8^{+1.5}_{-1.8}$	$28.8^{+0.3}_{-0.4}$	21.7
UGC 2319	$10.8^{+0.1}_{-0.2}$	$22.4^{+0.0}_{-0.0}$			$27.1^{+0.6}_{-0.9}$	$28.1^{+0.1}_{-0.2}$	19.0
UGC 2418	$9.6^{+0.2}_{-0.2}$	$22.1^{+0.0}_{-0.0}$			$25.4^{+1.7}_{-2.4}$	$28.1^{+0.4}_{-0.7}$	17.7
UGC 12183	$5.3^{+0.4}_{-0.5}$	$22.8^{+0.1}_{-0.2}$			$17.4^{+1.2}_{-1.2}$	$28.9^{+0.4}_{-0.4}$	10.0
UGC 12208	$5.6^{+0.1}_{-0.1}$	$22.7^{+0.0}_{-0.0}$	$13.4^{+0.9}_{-2.9}$	$27.7^{+0.6}_{-1.9}$			9.3
UGC 12709	$12.7^{+0.1}_{-0.1}$	$24.8^{+0.0}_{-0.0}$	$19.6^{+0.7}_{-1.3}$	$27.9^{+0.3}_{-0.6}$			13.0

Table 3. The position R and surface brightness μ at the onset of the haloes, breaks and truncations in our galaxy sample. The positions are in kpc. The surface brightness is in r' -mag/arcsec².

Galaxy	Inner galaxy		Outer galaxy		Truncation		Halo	
	h	μ_0	h	μ_0	h	μ_0	h	μ_0
IC 1515	$5.8^{+0.1}_{-0.1}$	$20.5^{+0.0}_{-0.0}$	$3.1^{+0.1}_{-0.1}$	$17.9^{+0.2}_{-0.3}$			$16.9^{+5.4}_{-4.1}$	$26.9^{+0.6}_{-0.8}$
IC 1516			$6.4^{+0.2}_{-0.2}$	$20.3^{+0.2}_{-0.2}$	$4.3^{+1.0}_{-0.7}$	$16.6^{+2.4}_{-2.6}$		
NGC 450	$3.7^{+0.1}_{-0.1}$	$21.2^{+0.0}_{-0.0}$	$1.3^{+0.0}_{-0.1}$	$15.8^{+0.3}_{-0.4}$			$5.2^{+1.5}_{-1.1}$	$25.1^{+0.9}_{-1.0}$
NGC 493	$6.0^{+0.2}_{-0.1}$	$20.6^{+0.0}_{-0.0}$	$2.5^{+0.1}_{-0.1}$	$17.3^{+0.1}_{-0.3}$			$13.6^{+2.9}_{-1.9}$	$26.4^{+0.5}_{-0.5}$
NGC 497	$13.1^{+1.1}_{-0.9}$	$20.5^{+0.1}_{-0.1}$	$6.6^{+0.2}_{-0.2}$	$18.6^{+0.2}_{-0.2}$			$28.5^{+2.1}_{-3.5}$	$26.3^{+0.2}_{-0.4}$
NGC 799	$17.3^{+1.2}_{-1.0}$	$22.3^{+0.1}_{-0.0}$	$3.2^{+0.2}_{-0.2}$	$16.5^{+0.5}_{-0.7}$			$14.0^{+4.9}_{-5.2}$	$26.6^{+0.9}_{-2.1}$
NGC 856			$5.2^{+0.0}_{-0.0}$	$20.7^{+0.0}_{-0.0}$				
NGC 941	$2.5^{+0.1}_{-0.1}$	$20.8^{+0.1}_{-0.1}$	$1.6^{+0.0}_{-0.0}$	$19.0^{+0.1}_{-0.1}$				
NGC 1090	$6.1^{+0.1}_{-0.1}$	$21.1^{+0.1}_{-0.1}$	$3.6^{+0.3}_{-0.3}$	$17.7^{+0.9}_{-0.8}$				
NGC 7398	$14.3^{+1.0}_{-0.8}$	$22.1^{+0.0}_{-0.0}$	$2.5^{+0.3}_{-0.3}$	$19.1^{+0.5}_{-0.5}$			$6.7^{+0.7}_{-0.5}$	$23.5^{+0.5}_{-0.4}$
UGC 139	$6.1^{+0.2}_{-0.2}$	$21.6^{+0.1}_{-0.1}$	$2.6^{+0.4}_{-0.4}$	$17.3^{+1.2}_{-1.6}$			$14.7^{+6.0}_{-4.5}$	$27.2^{+0.9}_{-1.3}$
UGC 272	$4.7^{+0.0}_{-0.0}$	$21.1^{+0.0}_{-0.0}$	$2.2^{+0.4}_{-0.5}$	$19.1^{+0.7}_{-1.3}$			$4.6^{+2.0}_{-0.7}$	$23.2^{+2.3}_{-1.3}$
UGC 651	$3.3^{+0.0}_{-0.0}$	$20.9^{+0.0}_{-0.0}$	$1.6^{+0.4}_{-0.3}$	$17.9^{+1.2}_{-1.6}$			$4.3^{+1.5}_{-0.6}$	$23.6^{+1.6}_{-0.9}$
UGC 866			$1.1^{+0.0}_{-0.0}$	$20.2^{+0.1}_{-0.1}$			$16.0^{+5.0}_{-7.1}$	$28.4^{+0.2}_{-0.5}$
UGC 1934	$6.8^{+0.0}_{-0.0}$	$19.4^{+0.0}_{-0.0}$	$5.2^{+0.3}_{-0.3}$	$18.1^{+0.4}_{-0.4}$			$22.8^{+1.4}_{-1.2}$	$24.7^{+0.2}_{-0.2}$
UGC 2081	$3.3^{+0.0}_{-0.0}$	$21.5^{+0.0}_{-0.0}$	$1.7^{+0.1}_{-0.1}$	$17.6^{+0.4}_{-0.4}$				
UGC 2311	$7.3^{+0.4}_{-0.3}$	$21.2^{+0.1}_{-0.1}$	$3.3^{+0.1}_{-0.1}$	$18.0^{+0.2}_{-0.2}$			$17.5^{+6.0}_{-9.3}$	$26.8^{+0.6}_{-2.4}$
UGC 2319	$5.3^{+0.0}_{-0.0}$	$20.2^{+0.0}_{-0.0}$	$3.1^{+0.1}_{-0.1}$	$18.6^{+0.1}_{-0.1}$			$13.2^{+3.3}_{-2.7}$	$25.9^{+0.5}_{-0.7}$
UGC 2418	$7.7^{+0.3}_{-0.3}$	$20.8^{+0.0}_{-0.0}$	$2.9^{+0.1}_{-0.1}$	$18.5^{+0.2}_{-0.2}$			$8.0^{+2.7}_{-1.7}$	$24.7^{+1.1}_{-1.2}$
UGC 12183	$2.9^{+0.0}_{-0.0}$	$20.8^{+0.0}_{-0.0}$	$2.1^{+0.1}_{-0.1}$	$20.1^{+0.1}_{-0.1}$			$6.3^{+1.2}_{-0.8}$	$25.9^{+0.7}_{-0.7}$
UGC 12208	$6.6^{+0.4}_{-0.3}$	$21.7^{+0.0}_{-0.0}$	$1.7^{+0.0}_{-0.0}$	$19.0^{+0.1}_{-0.1}$	$0.8^{+0.4}_{-0.2}$	$19.0^{+0.1}_{-0.1}$		
UGC 12709	$7.9^{+0.2}_{-0.2}$	$23.0^{+0.0}_{-0.0}$	$2.4^{+0.1}_{-0.1}$	$19.0^{+0.2}_{-0.2}$	$1.5^{+0.2}_{-0.2}$	$19.0^{+0.2}_{-0.2}$		

Table 4. Fitted scale lengths in kpc and central brightness in r' -mag/arcsec² as measured from the ellipse profiles

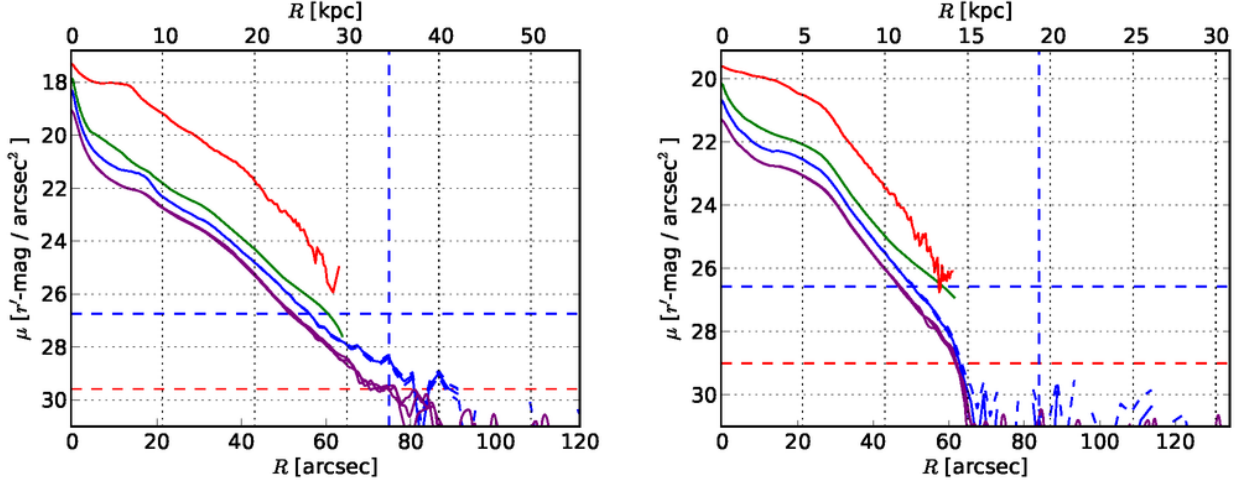


Figure 5. Full set of profiles for two examples galaxies, IC 1515 and UGC 12208. The red upper profile is from the PAS and the green is from the EP. The blue lines are the conventional ellipse fitting profiles. These are offset by +0.5 mag. The purple profiles show the results of the RPP applied at surface brightnesses of 25, 26 and 27 mag/arcsec²; these are offset by +1.0 mag. The dashed blue vertical lines denote the maximum radius used for the PAS and EP profile extraction. The dashed horizontal blue lines represent the 1σ standard deviation in the pixel-to-pixel noise and the red dashed horizontal lines the uncertainty limit.

of these regions we have a set of radii R and observed surface brightness levels $\mu_{\text{obs}}(R)$, to which we fit a linear relation with scale length h and central brightness μ_0 at $R = 0$ of form

$$\mu(R; \mu_0, h) = \mu_0 + 1.086 \frac{R}{h}. \quad (3)$$

The fits were performed on the ellipse-fitting profiles, as the EP profiles in general do not extend sufficiently far out, the PAS profiles suffer from convolution and the RPP results have been produced by stretching and compressing the data.

We give the fitting algorithm the freedom to estimate the noise by itself, in a method inspired by the use of the jitter parameter in Hou et al. (2012). We assume that the probability density p for parameters μ_0 and h is given by the Gaussian likelihood function

$$p = \prod_{R_i}^{R_N} \frac{1}{\sqrt{2\pi\sigma^2}} \exp\left(-\frac{[\mu(R_i) - \mu_{\text{obs}}(R_i)]^2}{2\sigma^2}\right), \quad (4)$$

where R_N is the collection of all measurements at positions R_i in the fitting region. It was assumed that the dispersion σ is not a function of radius along the profiles. The log-likelihood $\ln p$ is then

$$\ln p = -\frac{1}{2} \sum_{R_i}^{R_N} \left(\frac{[\mu(R_i; \mu_0, h) - \mu_{\text{obs}}(R_i)]^2}{2\sigma^2} n \right. \\ \left. + \ln(2\pi\sigma^2) \right), \quad (5)$$

$$\approx -\frac{1}{2} \sum_{R_i}^{R_N} \left(\frac{[\mu(R_i; \mu_0, h) - \mu_{\text{obs}}(R_i)]^2}{2\sigma^2} \right. \\ \left. + \ln(\sigma^2) \right), \quad (6)$$

where we drop the 2π term as it is only a constant and does not influence the outcome. Setting $\ln p = -1/2\chi^2$, we then

have

$$\chi^2 = \sum_{R_i}^{R_N} \left(\frac{[\mu(R_i; \mu_0, h) - \mu_{\text{obs}}(R_i)]^2}{2\sigma^2} + \ln(\sigma^2) \right). \quad (7)$$

We perform an initial fit to the data by minimizing χ^2 , using the PYTHON routine SCIPY.OPTIMIZE.LEASTSQ. After we had achieved a proper fit, we switched to a Markov-Chain Monte-Carlo (MCMC) sampler, EMCEE, to estimate the posterior likelihood distribution $\ln p$ and the distribution in each of the parameters (Foreman-Mackey et al. 2013). We used 300 separate walkers, which after a burn-in period of 50 iterations, sample the data for 500 iterations, giving 135000 samples. For each parameter, the median value (50%) of that parameter distribution is used as the reported value, while the upper and lower errors are reported based on the 16% and 84% parts of the distribution. The radii of the breaks and truncations were calculated using the intersection of both sets of samples, with the error derived in the same way as before. These radii were used to calculate the brightness, which is the brightness of the profile at the onset of that feature at position R . We demonstrate this in the left panel of Figure 6.

This method was insufficient for the halo, as the halo lies ‘on top’ of the regular stellar disc profile. We thus fit the combined profile of both the stellar profile ($\mu_{0,s}, h_s$) and the halo ($\mu_{0,h}, h_h$). For this, we used the combination of both fitting regions, as well as the region between these two. The combined profile is given by

$$\mu(R; \mu_{0,s}, h_s, \mu_{0,h}, h_h) = \ln \left[e^{\mu(R; \mu_{0,s}, h_s)} + e^{\mu(R; \mu_{0,h}, h_h)} \right]. \quad (8)$$

We used the parameters from the individual line segment fits as initial values and again performed the subsequent MCMC analysis using EMCEE. The brightness μ of the halo onset was calculated from the brightness of only the halo, rather than from the combination of halo and stellar disc.

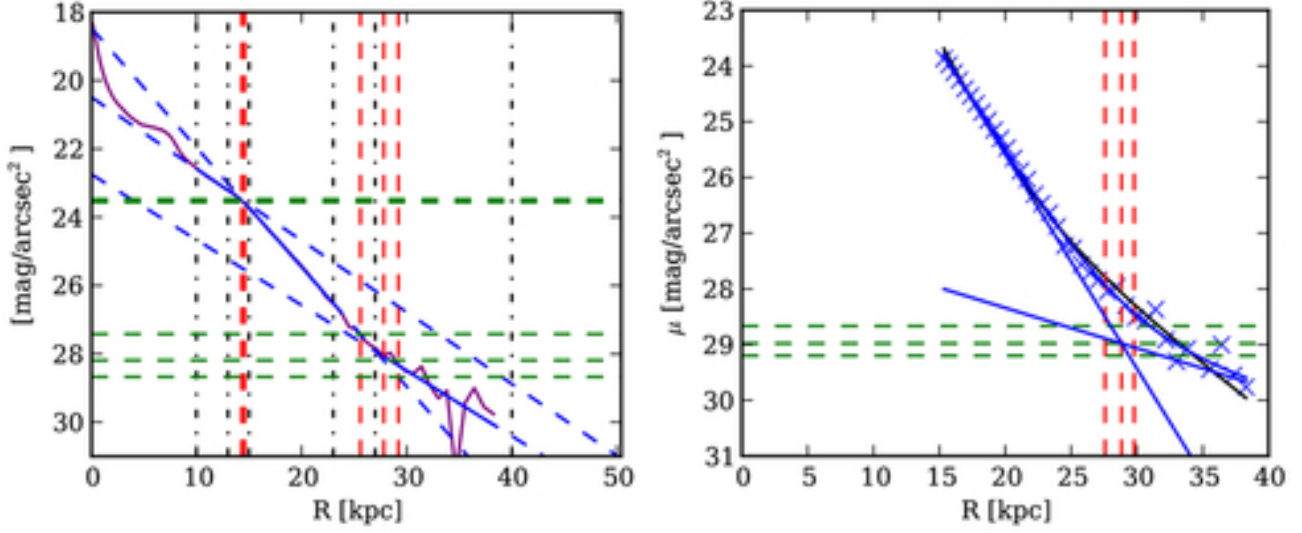


Figure 6. Left panel shows the fitting of the profile of IC 1515 in three different sections, for a break and a halo. The red vertical dashed lines denote the estimation of the position R and uncertainty for each feature. The green horizontal lines show the central position and errors on the brightness μ . The vertical black dash-dotted lines show the outer boundaries of the fit regions. The right panel shows the improved fit to the halo. See the text for more details.

We demonstrate the new combined fit in the right panel of Figure 6. The combined fits for all profiles can be found in the Appendix in Figures A23 and A24.

The total luminosity of the galaxy L_{total} was measured by integrating the profile $\mu_0(R)$ (in counts) up to the trust radius R_{trust} :

$$L_{\text{total}} = \int_{R=0}^{R_{\text{trust}}} 2\pi R(1-e)10^{-0.4\mu_{\text{obs}}(R)} dR. \quad (9)$$

The ellipticity term e is used to correct for the inclination. The total luminosity ($R \rightarrow \infty$) of the flattened halo L_{halo} is

$$L_{\text{halo}} = 2\pi h_{\text{h}}^2(1-e)10^{-0.4\mu_{0,\text{h}}}. \quad (10)$$

Here h and μ_0 are the scale length and central brightness as measured for the halo. We are interested in what fraction η of the total luminosity originates from the halo. Because L_{halo} as defined in Equation 10 runs to infinity, while L_{total} only integrates up to R_{trust} , we need to correct for this missing light, as follows:

$$\begin{aligned} \eta &= \frac{L_{\text{halo}}}{L_{\text{total}}} [R \rightarrow \infty], \\ &= \frac{L_{\text{halo}}}{L_{\text{total}} [R \leq R_{\text{trust}}] + L_{\text{halo}} [R > R_{\text{trust}}]} [R \rightarrow \infty], \end{aligned} \quad (11)$$

where we assume that the only light beyond R_{trust} originates from the halo component, such that

$$\begin{aligned} L_{\text{halo}} &= 2\pi h_{\text{h}}10^{-0.4\mu_{0,\text{h}}} \exp\left(-\frac{R_{\text{trust}}}{h_{\text{h}}}\right) (h_{\text{h}} + R_{\text{trust}}) \\ & [R > R_{\text{trust}}]. \end{aligned} \quad (12)$$

The radii and brightness levels for the breaks, haloes and truncations are shown in Table 3, the measured scale lengths are shown in Table 4 and the halo light fractions η are shown in Table 5.

Galaxy	Morphological type	M_{abs}	η
IC 1515	Sb	-21.9	$0.020^{+0.005}_{-0.007}$
IC 1516	Sbc	-22.2	
NGC 450	SABc	-19.8	$0.058^{+0.020}_{-0.022}$
NGC 493	Sc	-20.4	$0.031^{+0.006}_{-0.006}$
NGC 497	SBbc	-22.7	$0.025^{+0.002}_{-0.004}$
NGC 799	Sba	-22.0	$0.019^{+0.007}_{-0.016}$
NGC 856	SABc	-21.8	
NGC 941	SABc	-19.5	
NGC 1090	Sbc	-21.3	
NGC 7398	SABc	-21.0	$0.152^{+0.031}_{-0.023}$
UGC 139	SABc	-20.5	$0.023^{+0.008}_{-0.012}$
UGC 272	SABc	-19.6	$0.176^{+0.161}_{-0.088}$
UGC 651	Sc	-19.2	$0.155^{+0.096}_{-0.055}$
UGC 866	Sd	-17.2	$0.123^{+0.009}_{-0.021}$
UGC 1934	Sbc	-21.9	$0.094^{+0.007}_{-0.007}$
UGC 2081	SABc	-19.0	
UGC 2311	Sb	-22.0	$0.023^{+0.005}_{-0.023}$
UGC 2319	Sc	-20.7	$0.038^{+0.008}_{-0.010}$
UGC 2418	SABb	-21.3	$0.056^{+0.025}_{-0.026}$
UGC 12183	Sbc	-19.5	$0.049^{+0.014}_{-0.013}$
UGC 12208	Scd	-19.7	
UGC 12709	SABm	-19.1	

Table 5. Absolute brightness for each galaxy and the halo light fraction η . The values for M_{abs} refer to the r' -band.

4.2 Notes on Individual Galaxies

The vast majority (91%) of our sample shows some form of break in their light profile. These can be “classical” breaks (86%), and/or truncations (14%) at much lower surface brightness levels, with only NGC 856 and UGC 866 showing no indication of a break or a truncation. The most distinct truncation in the sample is seen in UGC 12208. Only NGC 856 has a pure exponential disc.

IC 1515, IC 1516, and NGC 799 have the lowest incli-

nations of the sample. Between the three of them, breaks, haloes, and truncations have all been detected, explicitly showing the feasibility of detecting these features in face-on galaxies. Conversely, all the highly inclined ($i > 70$ deg) galaxies of our sample (NGC 493, UGC 651, UGC 866, UGC 1934, and UGC 2319), feature apparent stellar haloes yet none displays a truncation.

Four galaxies from our sample overlap with the sample of Pohlen & Trujillo (2006). For NGC 450, NGC 941, and UGC 12709 both studies agree on the occurrence of a break as well as the radius at which it is observed. For UGC2081, there is a disagreement; we did not detect the break they find at $53''$. However, they did note that “downbending break” starts “clearly at 70 arcsec”. This galaxy was also analyzed by Bakos & Trujillo (2012), who report a break at $66.5''$ from r' -band profiles, while we report $71''$.

Further agreement with the literature is found for the barred spiral UGC 2311. The break found at $37''$ is broadly consistent with Bakos & Trujillo (2012), who report it at $42''$. Additionally, NGC 941 was also analyzed by Muñoz-Mateos et al. (2013) in the mid-infrared at 3.6μ , where they report a break at $80''$, while we report $61''$.

5 DISCUSSION

5.1 Comparing the Various Techniques

We have used four different methods to analyze the profiles. Ellipse profiles have a well-established history and set the standard for surface photometry. The EP, which was already used long ago, and PAS methods were presented, applied and discussed in Peters et al. (2017). The EP is found to reproduce similar results as ellipse fitting in bright regions of the galaxy, but suffers more from background noise. The PAS method was developed as a way to project face-on galaxies to edge-on in order to detect truncations. The PAS method was found by Peters et al. (2017) to create a differently shaped profile. However, using these new profiles Peters et al. (2017) were unable to reproduce the correlations seen in the edge-on sample of Martín-Navarro et al. (2012), and so argued that no real truncations had been detected in the Peters et al. (2017) sample. In this paper, we introduce a fourth method, rectified polar profiles, inspired by the earlier work by Pohlen et al. (2002).

The images analyzed in this paper are two magnitudes deeper than the default SDSS images. The effect of this is clearly noticeable on the EP and PAS methods. These now extend to further radii and fainter surface brightness levels, although the pixel-to-pixels noise remains the limiting factor. As previously seen in Peters et al. (2017), the ellipse method remains superior at faint brightness levels, as the averaging over large areas allows it to measure reliably the profile below the pixel-to-pixel noise level. Similar to this, the polar rectified profiles also average over large areas and can thus reach the same limiting brightness levels.

Comparing the polar and ellipse profiles directly, we note that the results are often similar. This is expected, as non-rectified polar profiles are effectively the same as ellipse profiles. At faint brightness levels, the outer edges of galaxies are clearly wobbling, as previously noted by Pohlen et al. (2002). It was postulated by van der Kruit & Freeman (2011)

that these local variations are important when hunting for truncations. Our work here demonstrates this, as can be observed in Figure A1 (Appendix), where the ellipse profile displays a bump in the profile, yet the rectified polar plots show that the profile is actually dropping towards the sky at a constant rate.

In conclusion, we find that the PAS and EP methods are ill suited for the detection of truncations. They should only be used in brighter parts of galaxies. Rectified polar and ellipse profiles are on par in terms of the limiting magnitude. The rectified polar profiles demonstrate that it is important to take the ragged or lopsided nature of galaxies into account, as the ellipse method is averaging these features out.

5.2 Possible PSF Effects

As argued by de Jong (2008) and Sandin (2014, 2015), the point spread function (PSF) in SDSS images can lead to a significant contribution of scattered light in the outer regions of galaxies. This is in particular true for highly inclined objects, where the minor axis is much shorter than the major axis, and light from the inner parts of a galaxy can thus be scattered to larger projected radii more easily. We are typically reaching the 29-30 r' -mag/arcsec² depth in our profiles. What is the effect of the point spread function at these depths on the profiles? To test this, we will generate synthetic galaxies based on the fitted scale lengths of IC 1515, NGC 493 and UGC 2418. These galaxies have been selected based on their size and inclination; together they represent a cross-section of the various types of galaxies in this sample.

For this one needs to know the PSF to very faint levels. A first study was performed in Peters (2014) with a carefully built PSF using well over 10000 stars observed in various g' , r' and i' averaged images with the SExtractor and PSFEX tools. This gave the PSF up to a radius of $177''$. The PSF images were convolved with a synthetic image using the ASTROPY.CONVOLUTION.CONVOLVE package for the convolution, which is a non-FFT convolution algorithm (Astropy Collaboration et al. 2013). Then ELLIPSE was used on on both the original and convolved synthetic image to extract their profiles. The result of that was presented as Figure 7.5 in Peters (2014) and the conclusion from that was that the PSF can seriously affect the outer surface brightness profile, but in general is insufficient to be the only cause of the apparent extended stellar halo.

In the mean time a better PSF was determined using bright stars in addition to a very large number of faint stars (Fliri & Trujillo 2016). With this a new analysis of the outer parts of galaxies and the reality of the apparent extended stellar haloes is possible (Kelvin et al. 2015). Here we report the result of such an analysis on the same three galaxies as in Peters (2014), using a 2001×2001 PSF.

First, automated routines to perform image cutting, PSF-resizing, source detection, secondary source masking and initial parameter estimation are employed for each galaxy via methods similar to those presented in (Kelvin et al. 2012). These data products are subsequently used to fit a 2D model to each source using the Imfit software (Erwin 2015). A Sersic + Broken Exponential model is fit using a smaller 255×255 pixel PSF, for speed. Loosely speak-

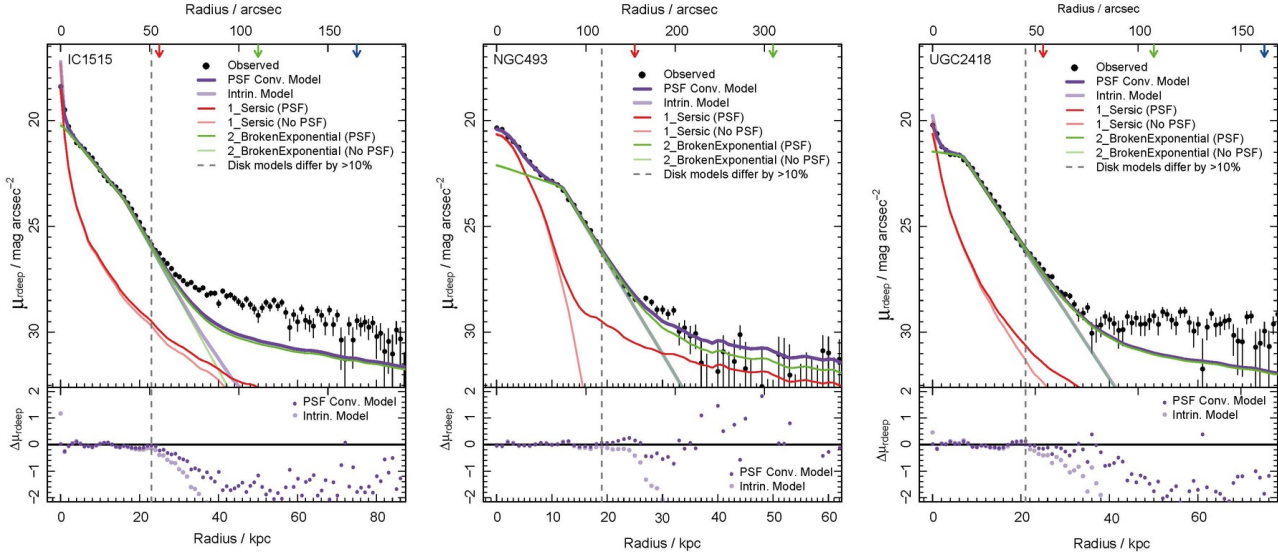


Figure 7. Test whether the PSF can create an artificial halo. The red lines are a Sérsic fit to the inner galaxy, corresponding to the bulge, the light line before and the dark line after convolution with the PSF. The green lines a broken exponential, again before and after convolution. The purple lines correspond similarly the sum of the two. The grey line indicates the minimum radius where the models differ by more than 10% from the observations. We have IC 1515 on the left, NGC 493 in the middle, and UGC 2418 at the right.

ing, these components can be interpreted as bulge and disc, respectively. The automated fitting outputs are saved, and used as an input for a manual fit with the larger 2001×2001 pixel PSF. Modifications are made to the model parameters to provide a more accurate estimation of the underlying galaxy flux. In order to facilitate this step, a plotting script generates a series of 2D images of the original galaxy, the model, and the sub-components, as well as a measure of the 1D surface brightness profile.

The final results are shown in Figure 7. The conclusion is the same as before. The PSF contamination contribution, defined as $[\text{flux}(\text{convolved}) - \text{flux}(\text{intrinsic})] / \text{flux}(\text{intrinsic})$, are 49% for NGC 493, 45% for UGC 2428 and 47% for IC 1515. It is thus clear that a significant amount of light in the halo is due to the PSF, as predicted by de Jong (2008) and Sandin (2014). In some cases, such as NGC 493, this apparent sterlight-like halo could be almost solely due to the PSF effect, while in others it could account for only a part the apparent stellar haloes.

5.3 Correlations

We have performed a wide range of tests on the various parameters associated with the galaxies to look for possible correlations. An overview of all the correlations, or lack thereof, is presented in Figure 8. We have found no correlation of either the radius of the feature or its brightness at that radius, with morphological type, apparent or absolute magnitude, radial velocity, distance, inclination, or maximum rotational velocity (see Table 1).

Our main, surprising, result is shown in Figure 10, where we show the radius R of the various types of feature against the radius at the 25th magnitude, R_{25} , of its host galaxy. A couple of interesting things can be noticed from this figure. First, there is a clear correlation of the break radius R_b with the size of the galaxy, with a best lin-

ear fit of $R_b = 0.77R_{25}$. A second, different correlation is that of the radii of the halos *and* truncations, R_h and R_t , with host galaxy size. Both features follows the combined linear relation $R_{h\&t} = 1.43R_{25}$ (see Figure 10 for a larger version of this plot). Measured separately, the linear fits become $R_h = 1.42R_{25}$ and $R_t = 1.52R_{25}$. Table 3 illustrates this relation between halos and truncations further. Halos and truncations are mutually exclusive: a galaxy has either a halo or a truncation.

In Figure 9 we present an overview of the correlation of the halo light fraction η with various other parameters of the galaxy. The halo light fraction correlates most strongly with the position at which the halo starts to dominate the profile, expressed as R/h , and the brightness of the halo at that position μ . These are unsurprising correlations, as a bright halo can be expected to dominate a profile at higher luminosities than a faint halo. More interesting is the lack of correlation with ellipticity e and maximum circular rotation V_{rot} of the galaxy. The relative brightness of the halo does not depend on inclination nor dynamical mass. The only other correlations are between the size R_{25} and absolute brightness M_{abs} of the galaxy, and the halo fraction. Fainter and smaller galaxies have the relatively largest haloes.

5.4 Breaks

We postulate that the breaks we see well within the discs of our sample galaxies occur in the general radial region where the star-forming spiral arms end. This can be recognized rather clearly in individual galaxies when comparing the radii of the breaks with the images of the galaxies, as shown in the appendix figures.

A similar distinction between breaks and truncations has been reported by Martín-Navarro et al. (2012) from their study of highly inclined galaxies. The results are not comparable in detail, because it is not clear how the end of a star-

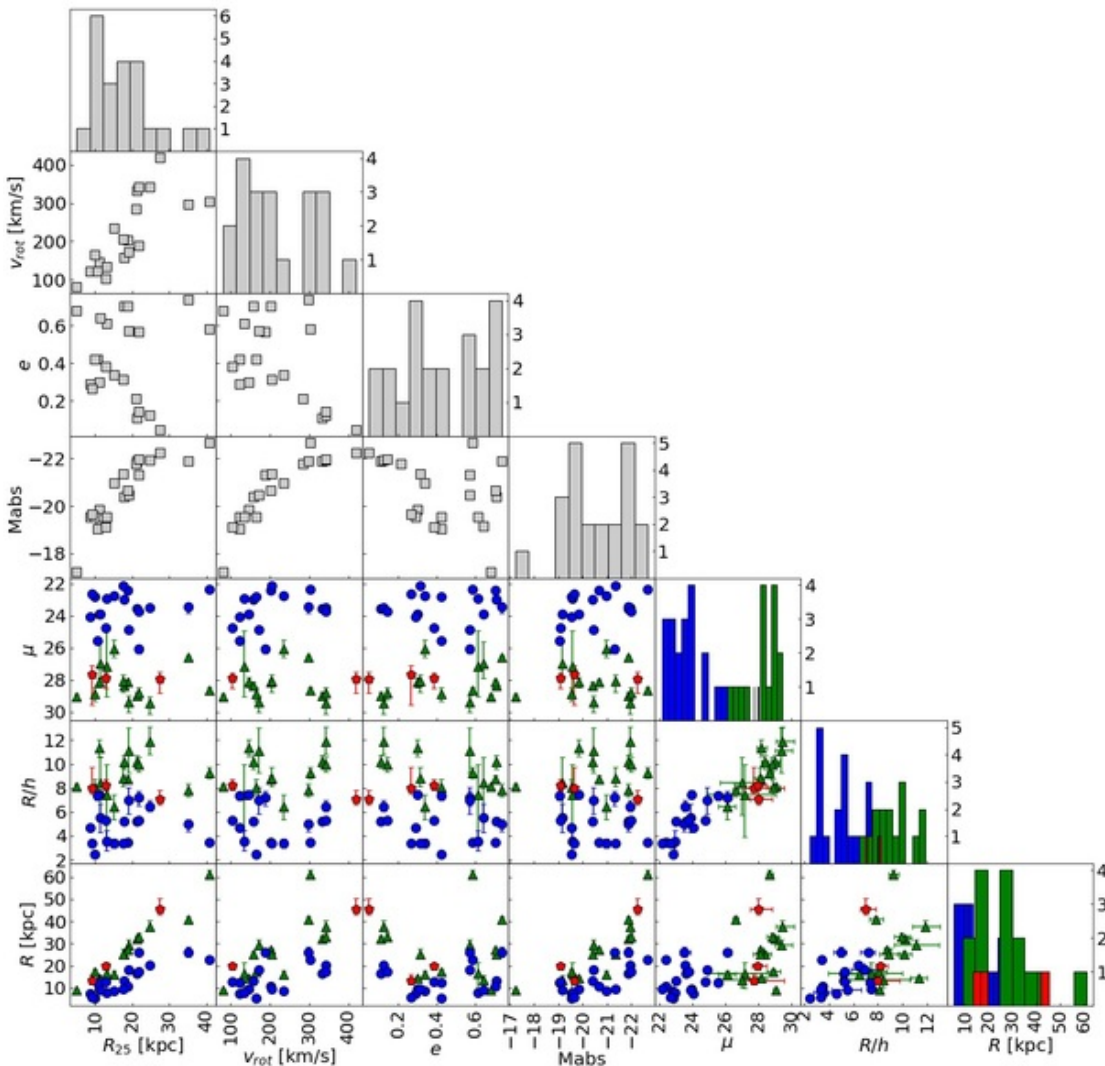


Figure 8. Overview of the correlations between various parameters. The absolute magnitude is in the r' -band. The brightness of the feature μ is in r' -mag/arcsec². Where multiple features are shown together the haloes are represented by green triangles, the breaks with blue circles and the truncations with red pentagons.

forming spiral arm zone is observed in an inclined galaxy, where dust obscuration and projection effects will hinder direct observations. Nevertheless, the typical radii and surface brightness levels for the breaks found by Martín - Navarro et al. (2012), of 7.9 kpc and 22.5 mag arcsec⁻², respectively, are compatible with the values we find here for face-on galaxies, 13.6 ± 6.4 kpc and 22.8 ± 2.8 r' -mag arcsec⁻². Selecting all variations of type II profiles in Pohlen & Trujillo (2006, Table 3), we find an average of 9.5 ± 3.9 kpc, which is again compatible.

We conclude that breaks at a level of around 23 r' -mag/arcsec² are very common in disc galaxies, and that in all cases there is a steeper slope after the break. Such breaks are most likely due to changes in the star formation properties. These occur as one changes from the regime of actively star-forming spiral arms to more quiescent parts of the disc. They may also be related to the star formation often occurring near the ends of a bar, which can lead to a rise in the radial profile, followed by a break as the radius moves out-

side the bar regime. Note that evidence for a break should not come from the rectified polar plots, but only from the ellipse fitting or the EPs.

In any case, we conclude that these disc breaks are unrelated to the truncations which we discuss elsewhere in this paper, and which we claim are the counterparts to the truncations reported since decades in edge-on galaxies. Claims in the literature of truncations (as well as anti-truncations) in face-on galaxies at or near the relatively high surface brightness levels identified here with disc breaks should not be confused or identified with truncations, nor should they be referred to as such.

5.5 Truncations

The criteria for the classification of the features in the outer parts at fainter levels than breaks are rather unambiguous. In order to test the presence of a truncation we exclusively examined the rectified polar plots and only accept evidence

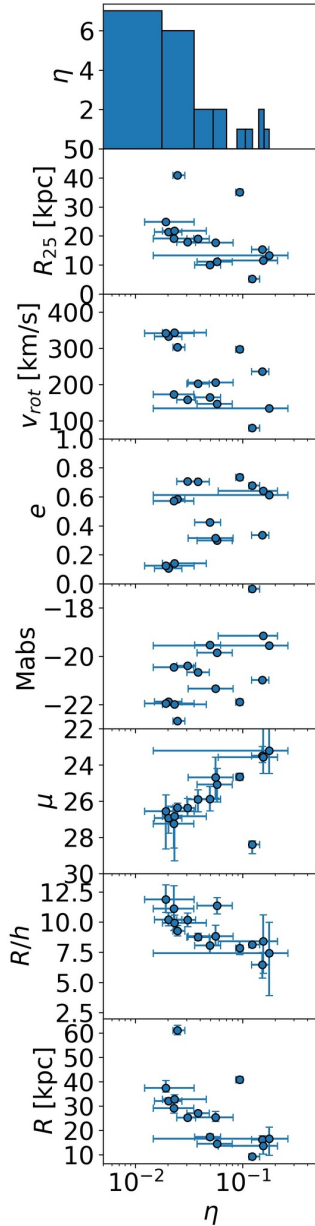


Figure 9. Overview of the correlations with the fraction of the total light from the galaxy that is emitted by the halo η . The absolute magnitude M_{abs} and the brightness of the halo μ are both in r' -mag/arcsec². The maximum rotation of the galaxy V_{rot} is in km/s. The ratio of the profile scale length h to the radius of the halo R/h is dimensionless.

for a truncation when a change in slope (down-bending) occurs at levels below 26 mag arcsec⁻² in at least one of the RPP the profiles. Any truncation should show up best when the isophote used for the rectification is close to the surface brightness where the truncation starts. Only in the case of NGC 799 do we see the profiles continue without any trace of a change in slope. In most cases there either is a clear downturn of the radial luminosity profile –and then we identify that as a truncation– or the profile flattens off and fades away into the noise quite slowly –the signature of a faint halo. The existence of a truncation need not be confirmed

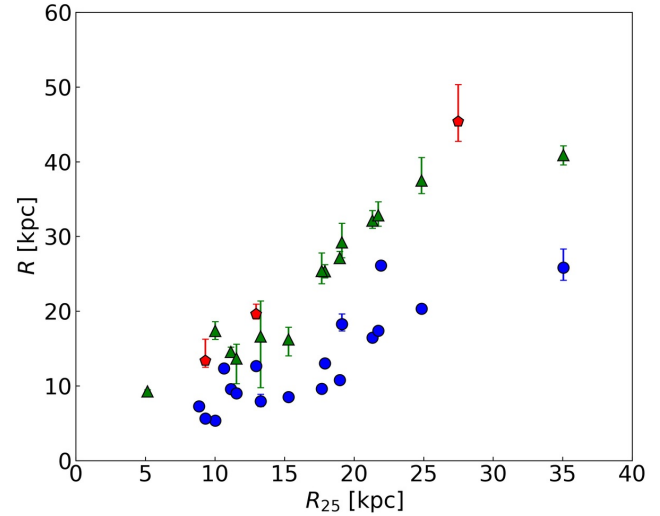


Figure 10. The correlation of the R_{25} , indicative of the size of a galaxy, with the various feature radii R . Red pentagons represent the truncations. Blue circles represent the breaks. Green triangles represent the haloes.

by requiring that it also occur in the other profiles. After all, the rectified polar plots were especially designed to optimally show truncations, but need not necessarily be absent in other methods, or in all other RPP profiles. It is true that in the PAS profiles, they should be present also, but in practice, those profiles can never be traced out far enough to do this confirmatory test.

In most cases (15 out of the 22 galaxies), there is very clear evidence of a change in slope in the profiles towards a slower decline with galactocentric radius at faint levels. This we identify with faint apparently stellar haloes. By the time the luminosity profiles of these haloes can be identified the surface brightness has fallen from 26.5 to 28 r' -mag/arcsec² (see Section 5.6). Among the remaining seven cases, there are four galaxies in which there is no indication for a faint stellar halo and where the luminosity profiles show no evidence for a downturn. Therefore, in these galaxies we have no indication for a truncation. In the remaining three cases, we have been able to identify truncations. Inspection of the polar plots suggests that the slopes and the surface brightness of the changes are such that if these systems were seen edge-on, they would show the same signature of a truncation as we indeed observe in real edge-ons. It may be of interest to comment on the similarity of the profiles of UGC 12208 and 12709 to the double-downbending profiles in Pohlen & Trujillo (2006) and Herrmann et al. (2013), in both of which one galaxies display such a feature. In NGC 4517A the second break occurs at a much brighter level and in DDO 125 is a much fainter dwarf galaxy than we have in our sample. So, we do not believe that this a phenomenon similar to our truncations.

The truncations reported here occur at radii of significantly more than the canonical 4.2 ± 0.5 scale lengths, reported by van der Kruit & Searle (1981a, 1982) in edge-on galaxies, and certainly the 3.6 ± 0.6 of Kregel & van der Kruit (2004). The best estimate of the face-on surface brightness at which truncations observed in edge-on systems in the Kregel & van der Kruit (2004) sample should become

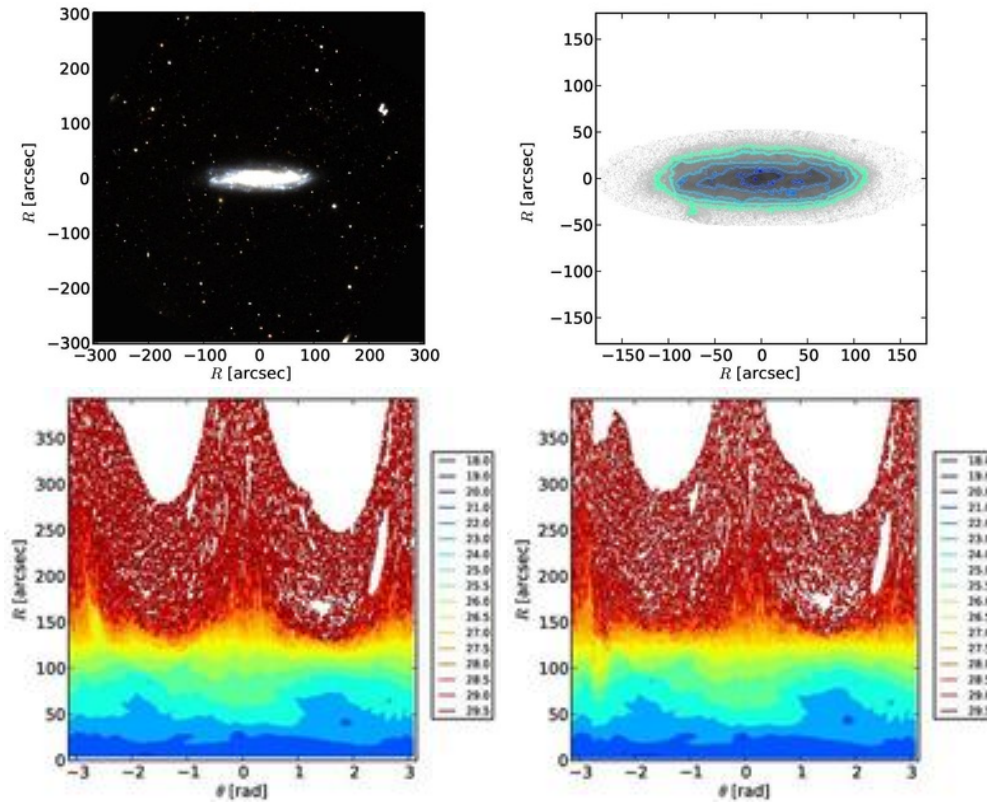


Figure 11. Polar plots for the highly inclined galaxy NGC 493. Note that the fainter levels of surface brightness extend further out along the minor axis at position angles 0 and π radians, even after rectification.

evident, would be of order 25.3 ± 0.6 R-mag arcsec $^{-2}$. Consistent with this, van der Kruit (2008) showed that the radii of the ‘classical truncations’ of Pohlen & Trujillo (2006) systematically occur at smaller radii than edge-on truncations in galaxies with the same rotation velocity. The truncations found in this paper thus occur at a larger number of scalelengths and at fainter surface brightnesses than in edge-on galaxies. This also holds when we use other samples of edge-on galaxies such as Pohlen et al. (2000). We have no real explanation for this; the only argument we can offer is that there may be serious problems comparing face-on and edge-on scalelengths and inferring face-on surface brightness levels from photometry in edge-on galaxies. The obvious difference is that in edge-ons the fitting is done above and below the dust lane and therefore excludes effects young populations and dust. It requires a separate investigation to address this fundamental issue.

The most straightforward interpretation would be that most or almost all galaxies have truncations of the sort we have found in three systems in this paper, but that their presence in inclined or face-on views is hidden by the presence of faint outer stellar haloes, in the way proposed by Bakos & Trujillo (2012) and Martín-Navarro et al. (2014). This halo may to some extent at least actually be due to PSF scattered light. In this case, the galaxy itself is hiding the presence of the truncation. On the other hand, if the absence of a detectable halo is unrelated to the presence or absence of a truncation then we are forced to conclude that three out of seven discs are truncated. For edge-on systems,

Kregel et al. (2002) and Kregel & van der Kruit (2004) found from a sample of 34 southern, edge-on spiral galaxies that at least 20 of these have radial truncations. The rest either have no truncations, or have them at a level inaccessible for us now. We have vindicated the prediction by Bakos & Trujillo (2012) that (spiral) galaxies usually –as judged from our sample, two-thirds of all galaxies– have faint stellar haloes that prevent the identification of a truncation.

5.6 Haloes

A natural prediction of the collapsing galaxy formation scenarios, in particular the hierarchical one, is the ubiquitous presence of stellar haloes surrounding galaxies (e.g. Eggen et al. 1962; Searle & Zinn 1978; Bekki & Chiba 2001; Samsland & Gerhard 2003; Steinmetz & Muller 1995). These extended and diffuse stellar components are formed from the debris of disrupted satellites accreted along the cosmic time (e.g. Bullock & Johnston 2005; Brook et al. 2003; Abadi et al. 2006).

In the local Universe, both based on integrated photometry (e.g. Bakos & Trujillo 2012) and on star counts (e.g. Barker et al. 2012), the outer regions of low-inclined disc galaxies ($R > 10$ kpc) are often characterized by an exponential surface brightness decrement followed by an excess of light over this exponential decay. This outer excess of light is located at $R \geq 20$ kpc and has surface brightness $\mu_R > 28$ mag arcsec $^{-2}$. These faint surface brightness levels are equivalent to the ones found in the literature using

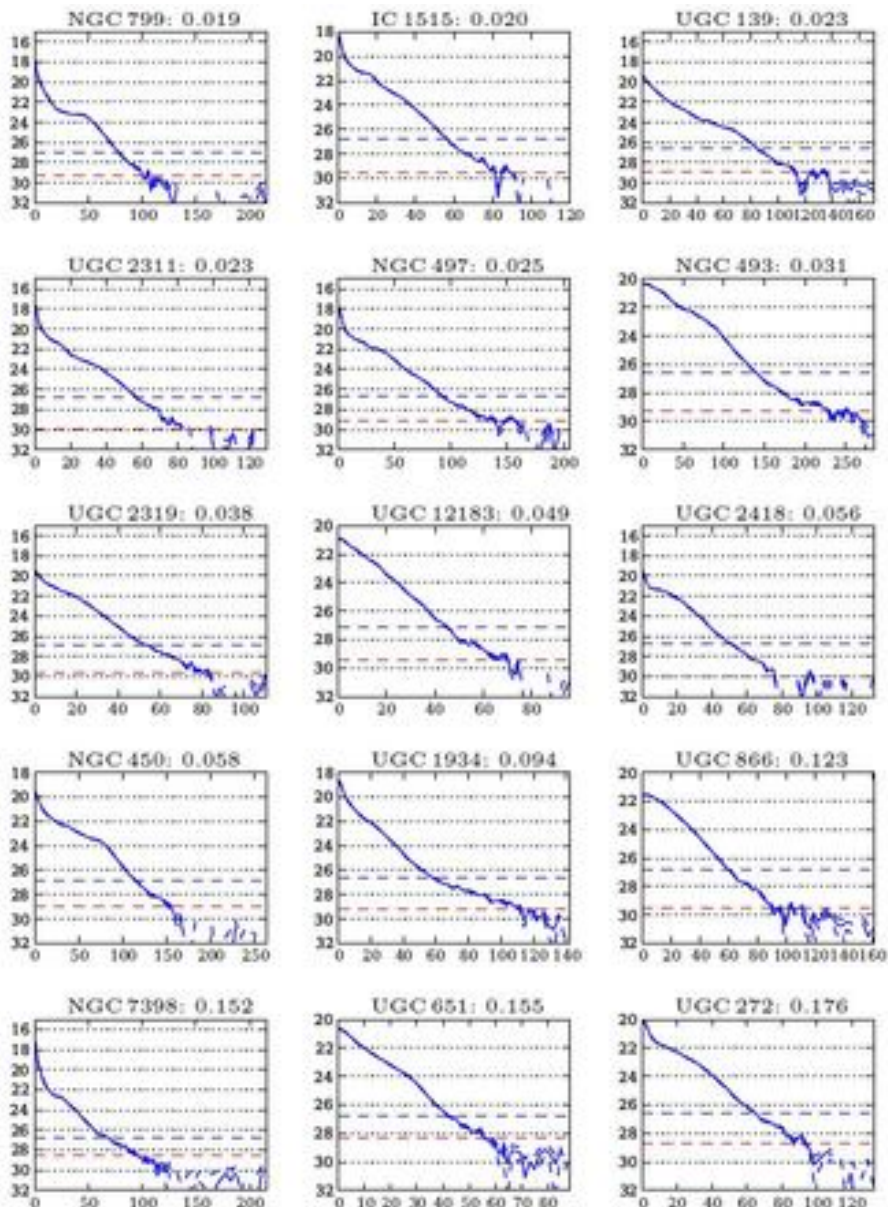


Figure 12. Profile mosaic depicting the increase of the halo light fraction η across the sample, the value of which is shown below each figure. The surface brightness μ in r' -mag/arcsec² on the vertical axis. The radius R in arcsec on the bottom horizontal axis.

galaxies with edge-on orientations at similar radial distances above the galactic planes. For instance, the edge-on spiral NGC 4565 has, along its minor axis, a surface brightness of $\mu_{6660} = 27.5$ mag arcsec⁻² (i.e., $\mu_R \sim 28$ mag arcsec² in the R-band) at 22 kpc above the disc (Wu et al. 2002). Similarly, Jablonka et al. (2010) found that the stellar halo of the edge-on disc NGC 3957 has a surface brightness of 28.5 mag arcsec⁻² in the R-band at 20 kpc above the disc plane. The similarity between these values in edge-on and face-on galaxies would entice us to conclude that we are observing the same component of the galaxy, i.e., their stellar halos.

A property of a stellar halo (and for that matter for the distribution of scattered light by the PSF) would be that it more or less spherical, independent of the inclination of the galaxy. It is the case that we fixed the ellipticity of the isophotes in the ellipse-fitting procedure, so we have no in-

formation on this in the outcome of these fits. In particular, in edge-on galaxies, the outer light should be more spherical than the galaxy. This should show up as faint extensions of the light distribution in the polar plots, even after rectification. And it should be most visible in highly inclined systems as extensions of the surface brightnesses at levels fainter than 27 or 28 mag arcsec⁻² in the RPP profiles near the minor axis (position angles 0 and π radians).

The two galaxies in Fig. 4 are too face-on to demonstrate this effect. But NGC 493 should serve as a good example, see Fig. 11. The fainter surface brightnesses indeed extend further out along the minor axis, indicating the the faint light has a more or less spherical distribution but stretched in the production of the polar plots, as expected for a stellar halo (but also for the case of scattered light). We see similar behaviour for the other highly inclined galax-

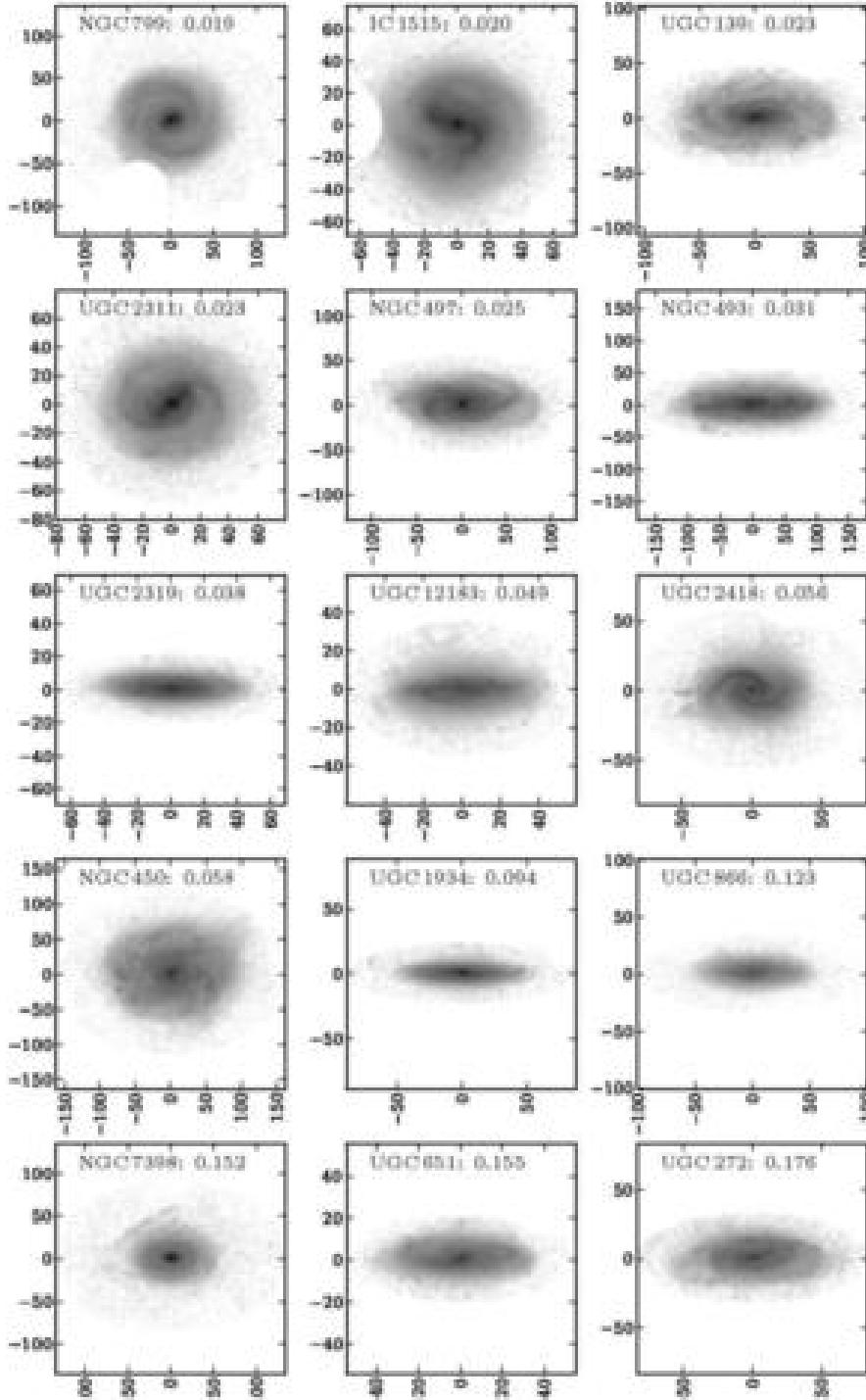


Figure 13. Image mosaic depicting the increase of the halo light fraction η across the sample, the value of which is shown in each figure. The axis scales are in arcsec.

ies in our sample, NGC 497, 1090, UGC 139, 272, 651, 866, 1934, 12183, 1218 and 32319 (see the figures in the online Appendix). To test this assertion further, we have attempted to perform ellipse fits to several of our galaxies, in which we let the ellipticity run free into the very outskirts. The aim was to demonstrate that the ellipticity increases towards these radii. Unfortunately, we find that the ellipse task fails to converge at the outskirts of galaxies.

We have demonstrated in Section 5.2 that for the three galaxies tested, the PSF scattered light of the galaxies was responsible for most or in one case even all of the observed halo. Further support for the importance of PSF scattering comes from a comparison of the fraction of light η in the ‘haloes’ and the total dynamical mass of the galaxies. It turns out that the two are essentially uncorrelated. This is at odds with numerical simulations, which predict that the

fraction of mass in stellar haloes should increase with total stellar mass (Cooper et al. 2013). As argued in Section 5.2, the smallest and faintest galaxies have the highest halo light fractions η . As an aid to the reader, in Figures 12 and 13 we demonstrate in two mosaics how the halo light fraction η increases in the sample.

Interestingly, our observed halo-light fractions (0.02-0.03) are already below the theoretical values of Cooper et al. (2013) (~ 0.1 ; their Fig. 12 for $B/T < 0.2$). However, there is room for explaining this discrepancy. First, our data could be selected against finding massive haloes. In fact, our sample of spiral galaxies is biased towards objects which do not have signatures of distortions caused by on-going or recent mergers. Second, we have studied the fraction of light of the haloes in the r' -band instead of the fraction of stellar mass, as done in the simulations. If, as expected, the stellar populations in the haloes are older than those in the galaxy discs, then our observed light fractions in the r' -band will be smaller than the stellar mass fractions. A rough estimate of this bias can be reached as follows. Assuming that the mean luminosity weighted age of the stellar population in the discs is 1-2 Gyr and in the stellar haloes 6-8 Gyr, then assuming a Solar metallicity and a Kroupa IMF, according to the Vazdekis et al. (2012) models we would get $M/L_{r'}$ (disc)=0.6-1.0 and $M/L_{r'}$ (stellar halo)=2.4-2.8. Consequently, our data (at least the observed offset between the fraction of light in the haloes and the theoretical expectation for the fraction of mass) could be in agreement with the numerical expectations.

Our result should serve as a warning for any future work: the effect of the PSF must be taken into account when attempting to interpret surface photometry of stellar haloes in face-on galaxies. The PSF will always play a major, limiting role in the detections. In this sense, a better and safer method for finding stellar haloes would be detecting individual stars, such as done by Radburn-Smith et al. (2011).

CONCLUSIONS

We present surface photometry of 22 nearby face-on and moderately inclined galaxies, from the IAC Stripe82 Legacy Project, using (co-)added data from the g' , r' and i' bands. Using traditional ellipse profiles, as well as our new rectified polar profiles, this allows us to probe down to a surface brightness level of 29-30 r' -magnitude / arcsec². Due to this, ellipse profiles smooth out any truncation that may occur and a special technique, introduced here and named rectified polar plots, is vital to detect them. For the first time ever, we have been able to detect truncations in three of our 22 face-on galaxies, using rectified polar profiles. Furthermore, we find that 15 other galaxies have apparent stellar haloes. Using synthetic galaxies convolved with a real PSF, we exclude the possibility that these haloes could be solely explained due to scattered light from the PSF. The light scattered by the PSF is, however, the dominant source of light in the outer parts of these galaxies. The presence of haloes and truncations is mutually exclusive, and we argue that the presence of a stellar halo and/or light scattered light by the PSF often outshines any truncation that might be present.

The radius of the onset of truncations and haloes cor-

relates tightly with the galaxy size, as measured with the R_{25} parameter. We find that the correlation is effectively the same for both features. We have also detected 17 breaks, which are found much closer to the centre of galaxies. Breaks are also found to correlate with the size of the galaxy, again measured with R_{25} . We have found no correlation between the colour or radius at the onset of breaks, truncations and stellar haloes, with morphological type, apparent or absolute magnitude, radial velocity and distance, inclination and maximum rotational velocity.

ACKNOWLEDGMENTS

SPCP is grateful to the Space Telescope Science Institute, Baltimore, USA, the Research School for Astronomy and Astrophysics, Australian National University, Canberra, Australia, and the Instituto de Astrofísica de Canarias, La Laguna, Tenerife, Spain, for hospitality and support during short and extended working visits in the course of his PhD thesis research. He thanks Roelof de Jong and Ron Allen for help and support during an earlier period as visiting student at Johns Hopkins University and the Physics and Astronomy Department, Krieger School of Arts and Sciences for this appointment.

PCK thanks the Instituto de Astrofísica de Canarias, La Laguna, Tenerife for hospitality during two visits supported by the Severo Ochoa mobility program, during which most of this work was performed. PCK is also grateful to the directors of the Space Telescope Science Institute in Baltimore, USA and the Research School of Astronomy and Astrophysics, Mount Stromlo Observatory, Australian National University at Canberra, Australia for hospitality during numerous work visits, of which a number were directly related to this research. He also acknowledges his local hosts Ron Allen, Ken Freeman and Johan Knapen for help and support.

We are grateful to Chris Sandin and Roelof de Jong for stressing the issue of the effects of the Point Spread Function.

We acknowledge financial support to the DAGAL network from the People Programme (Marie Curie Actions) of the European Union's Seventh Framework Programme FP7/2007-2013/ under REA grant agreement number PITN-GA-2011-289313, and from the Spanish Ministry of Economy and Competitiveness (MINECO) under grant numbers AYA2013-48226-C3-1-P (IT) and AYA2013-41243-P (JHK).

Work visits by SPCP and PCK have been supported by an annual grant from the Faculty of Mathematics and Natural Sciences of the University of Groningen to PCK accompanying of his distinguished Jacobus C. Kapteyn professorship and by the Leids Kerkhoven-Bosscha Fonds. PCK's work visits were also supported by an annual grant from the Area of Exact Sciences of the Netherlands Organisation for Scientific Research (NWO) in compensation for his membership of its Board.

REFERENCES

Abadi M. G., Navarro J. F., Steinmetz M., 2006, MNRAS,

- 365, 747
- Astropy Collaboration Robitaille T. P., Tollerud E. J., et al., 2013, *A&A*, 558, A33
- Bakos J., Trujillo I., 2012, ArXiv e-prints, ArXiv 204.3082)
- Barker M. K., Ferguson A. M. N., Irwin M. J., et al., 2012, *MNRAS*, 419, 1489
- Barteldrees A., Dettmar R.-J., 1994, *A&AS*, 103, 475
- Bekki K., Chiba M., 2001, *ApJ*, 558, 666
- Bertin E., Mellier Y., Radovich M., et al., 2002, in *Astronomical Data Analysis Software and Systems XI Vol. 281 of Astron. Soc. Pacific Conf. Ser.*, . p. 228
- Brook C. B., Kawata D., Gibson B. K., 2003, *MNRAS*, 343, 913
- Bullock J. S., Johnston K. V., 2005, *ApJ*, 635, 931
- Busko I. C., 1996, in *Jacoby G. H., Barnes J., eds, Astronomical Data Analysis Software and Systems V Vol. 101 of Astron. Soc. Pacific Conf. Ser.*, . p. 139
- Comerón S., Elmegreen B. G., Salo H., et al., 2012, *ApJ*, 759, 98
- Cooper A. P., D'Souza R., Kauffmann G., et al., 2013, *MNRAS*, 434, 3348
- de Jong R. S., 2008, *MNRAS*, 388, 1521
- de Jong R. S., Seth A. C., Radburn-Smith D. J., et al., 2007, *ApJ*, 667, L49
- de Vaucouleurs G., 1948, *Annales d'Astrophysique*, 11, 247
- Eggen O. J., Lynden-Bell D., Sandage A. R., 1962, *ApJ*, 136, 748
- Erwin P., 2015, *ApJ*, 799, 226
- Erwin P., Beckman J. E., Pohlen M., 2005, *ApJ*, 626, L81
- Erwin P., Pohlen M., Beckman J. E., 2008, *AJ*, 135, 20
- Ferguson A. M. N., Irwin M. J., Ibata R. A., Lewis G. F., Tanvir N. R., 2002, *AJ*, 124, 1452
- Fliri J., Trujillo I., 2016, *MNRAS*, 456, 1359
- Foreman-Mackey D., Hogg D. W., Lang D., Goodman J., 2013, *PASP*, 125, 306
- Freeman K. C., 1970, *ApJ*, 160, 811
- Fry A. M., Morrison H. L., Harding P., et al., 1999, *AJ*, 118, 1209
- Gutiérrez L., Erwin P., Aladro R., Beckman J. E., 2011, *AJ*, 142, 145
- Herrmann K. A., Hunter D. A., Elmegreen B. G., 2013, *AJ*, 146, 104
- Hou F., Goodman J., Hogg D. W., et al., 2012, *ApJ*, 745, 198
- Jablonka P., Tafelmeyer M., Courbin F., et al., 2010, *A&A*, 513, A78
- Jedrzejewski R. I., 1987, *MNRAS*, 226, 747
- Kelvin L., Trujillo I., et al., 2015, In preparation
- Kelvin L. S., Driver S. P., Robotham A. S. G., et al. 2012, *MNRAS*, 421, 1007
- Kregel M., Sancisi R., 2001, *A&A*, 376, 59
- Kregel M., van der Kruit P. C., 2004, *MNRAS*, 355, 143
- Kregel M., van der Kruit P. C., de Grijs R., 2002, *MNRAS*, 334, 646
- Laine J., Laurikainen E., Salo H., et al. 2014, *MNRAS*, 441, 1992
- Martín-Navarro I., Bakos J., Trujillo I., et al., 2012, *MNRAS*, 427, 1102
- Martín-Navarro I., Trujillo I., Knapen J. H., Bakos J., Fliri J., 2014, *MNRAS*, 441, 2809
- Meyer M. J., Zwaan M. A., Webster R. L., et al. 2004, *MNRAS*, 350, 1195
- Monachesi A., Bell E. F., Radburn-Smith D. J., Vlajić M., de Jong R. S., Bailin J., Dalcanton J. J., Holwerda B. W., Streich D., 2013, *ApJ*, 766, 106
- Muñoz-Mateos J. C., Sheth K., Gil de Paz A., et al., 2013, *ApJ*, 771, 59
- Oliphant T. E., , 2006, A Bayesian perspective on estimating mean, variance, and standard-deviation from data, <http://hdl.lib.byu.edu/187>
- Paturel G., Petit C., Prugniel P., et al., 2003, *A&A*, 412, 45
- Peters S. P. C., 2014, PhD thesis, Univ. Groningen
- Peters S. P. C., van der Kruit P. C., de Jong R. S., 2017, *MNRAS*, 464, 1591
- Pohlen M., Dettmar R.-J., Lütticke R., 2000, *A&A*, 357, L1
- Pohlen M., Dettmar R.-J., Lütticke R., Aronica G., 2002, *A&A*, 392, 807
- Pohlen M., Trujillo I., 2006, *A&A*, 454, 759
- Radburn-Smith D. J., de Jong R. S., Seth A. C., et al., 2011, *ApJS*, 195, 18
- Rix H.-W., Zaritsky D., 1995, *ApJ*, 447, 82
- Roediger J. C., Courteau S., Sánchez-Blázquez P., McDonald M., 2012, *ApJ*, 758, 41
- Samland M., Gerhard O. E., 2003, *A&A*, 399, 961
- Sandin C., 2014, *A&A*, 567, A97
- Sandin C., 2015, *A&A*, 577, A106
- Schlafly E. F., Finkbeiner D. P., 2011, *APJ*, 737, 103
- Searle L., Zinn R., 1978, *ApJ*, 225, 357
- Shostak G. S., van der Kruit P. C., 1984, *A&A*, 132, 20
- Springob C. M., Haynes M. P., Giovanelli R., Kent B. R., 2005, *APJS*, 160, 149
- Steinmetz M., Muller E., 1995, *MNRAS*, 276, 549
- Theureau G., Bottinelli L., Coudreau-Durand N. n. e., 1998, *AAPS*, 130, 333
- Trujillo I., Bakos J., 2013, *MNRAS*, 431, 1121
- van der Kruit P. C., 1976, *A&A*, 49, 161
- van der Kruit P. C., 1979, *A&AS*, 38, 15
- van der Kruit P. C., 1988, *A&A*, 192, 117
- van der Kruit P. C., 2008, in *Formation and Evolution of Galaxy Disks Vol. 396 of Astron. Soc. Pacific. Conf. Ser.*, . p. 173
- van der Kruit P. C., Freeman K. C., 2011, *ARA&A*, 49, 301
- van der Kruit P. C., Searle L., 1981a, *A&A*, 95, 105
- van der Kruit P. C., Searle L., 1981b, *A&A*, 95, 116
- van der Kruit P. C., Searle L., 1982, *A&A*, 110, 61
- Vazdekis A., Ricciardelli E., Cenarro A. J., et al., 2012, *MNRAS*, 424, 157
- White S. D. M., Rees M. J., 1978, *MNRAS*, 183, 341
- Wu H., Burstein D., Deng Z., et al., 2002, *AJ*, 123, 1364
- Zaritsky D., Rix H.-W., 1997, *ApJ*, 477, 118
- Zaritsky D., Salo H., Laurikainen E., et al., 2013, *ApJ*, 772, 135
- Zibetti S., Ferguson A. M. N., 2004, *MNRAS*, 352, L6
- Zibetti S., White S. D. M., Brinkmann J., 2004, *MNRAS*, 347, 556

APPENDIX A: OVERVIEW OF INDIVIDUAL GALAXIES

The following panels show our results for the individual galaxies.

In the top-left panel all surface brightness profiles are shown. The blue line shows the conventional ellipse profile. **To show the uncertainty created by noise, we determined the ellipse profiles two additional times. In the first, we added the pixel-to-pixel noise to the image, while in the second we subtracted this amount. We show these two additional profiles by dashed blue profiles.** Offset by +0.5 mag are the equivalent profiles, in green. Three versions of corrected polar profiles (using rectification at 25, 26 and 27 magnitudes arcsec^{-2} , respectively) are shown in purple with an offset of -0.5 mag. The PAS profiles are shown in red and are offset +1 mag from the central value of the ellipse profiles. We note that the PAS are in pseudo r' -mag/ arcsec^2 and do not represent the same scale as the other profile (see above for more details). The dashed blue vertical line denotes the maximum radius used for the PAS and EP profile extraction. The dashed horizontal blue line represents the 1σ standard deviation in the pixel-to-pixel noise (see section 3). The red dashed horizontal line represents the uncertainty limit. We use the Python BAYES_MVS package to establish the confidence limits on the background zeropoint. The BAYES_MVS package provides a 90% confidence range for this zeropoint. We define the uncertainty limit as the upper confidence limit of this range. This provides a natural limit to the accuracy, below which the uncertainty in the background zeropoint is too high for any reliable profile. The top-right panel shows the sky in counts as seen from the elliptical profiles. In the second row we show on the left side a RGB image produced from the g' , r' and i' images, rotated such that the major axis of the galaxy aligns with the horizontal axis. The scale for all images is in arcsec unless otherwise noted. On the right side we show the uncorrected background of the (co-)added image, smoothed by a Gaussian with a radius of three pixels. The image is again aligned to the major axis of the galaxy. The colours range from -0.5 to 0.5 ADU. The green contour represents a outer cutout region from the larger raw image. The ticks beside each image are in arcsec. The left panel on the third row shows the corrected background in the cutout region. The scale again ranges from -0.5 to 0.5 ADU. No smoothing is applied. The blank holes are due to the mask. The blue ellipse shows the ellipse used as a limit for the PAS and EP methods. The right panel on the third row shows the cutout ellipse of the PAS and EP methods. The scale has been optimized to show the faint outer regions of the galaxy. The contours match the colourbars on the last row. The last row shows two versions of the polar profiles, with on the left the uncorrected profile, and on the right the effect of a rectification at a level of 26 magnitudes / arcsec^2 .

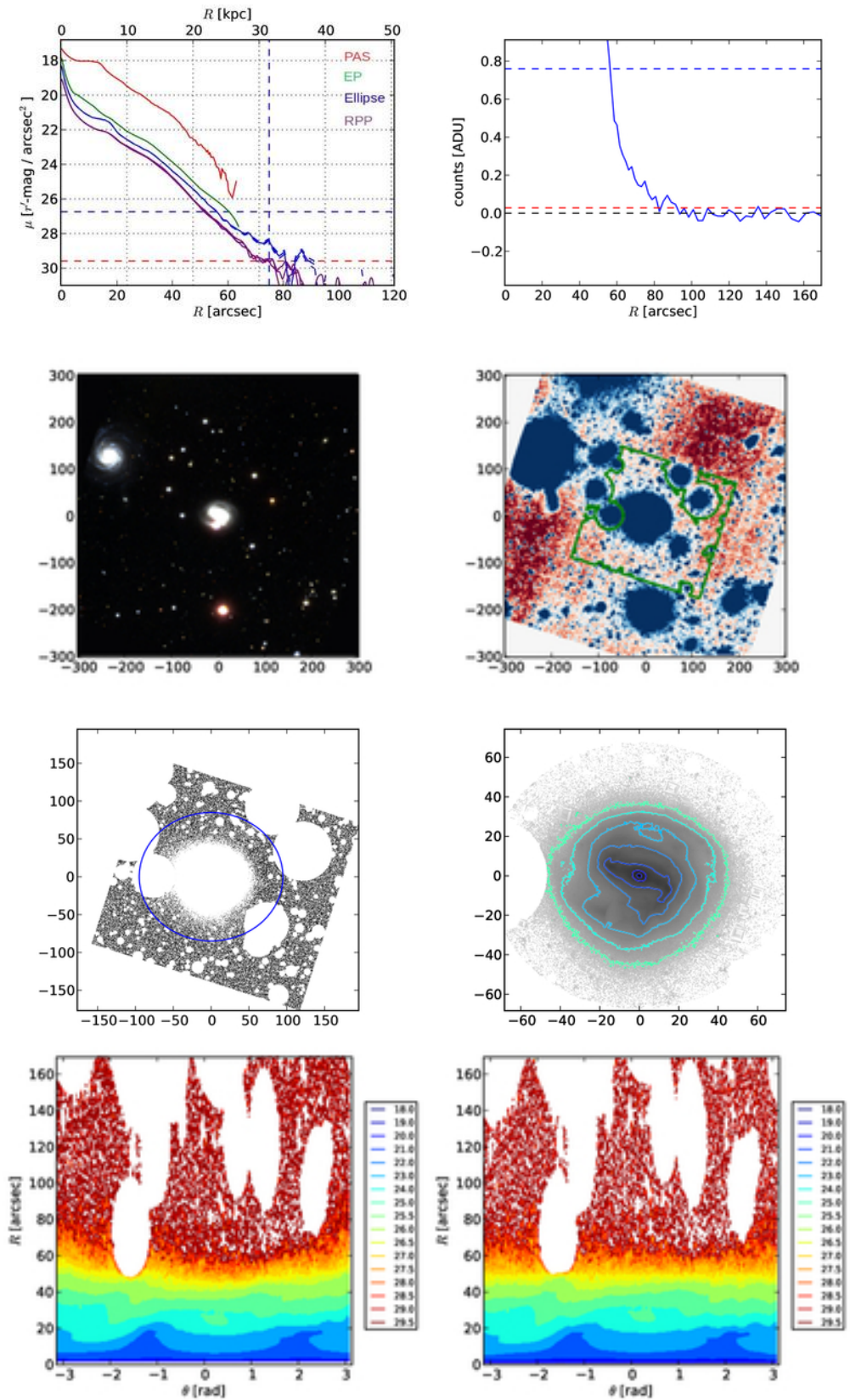


Figure A1. Results for IC 1515.

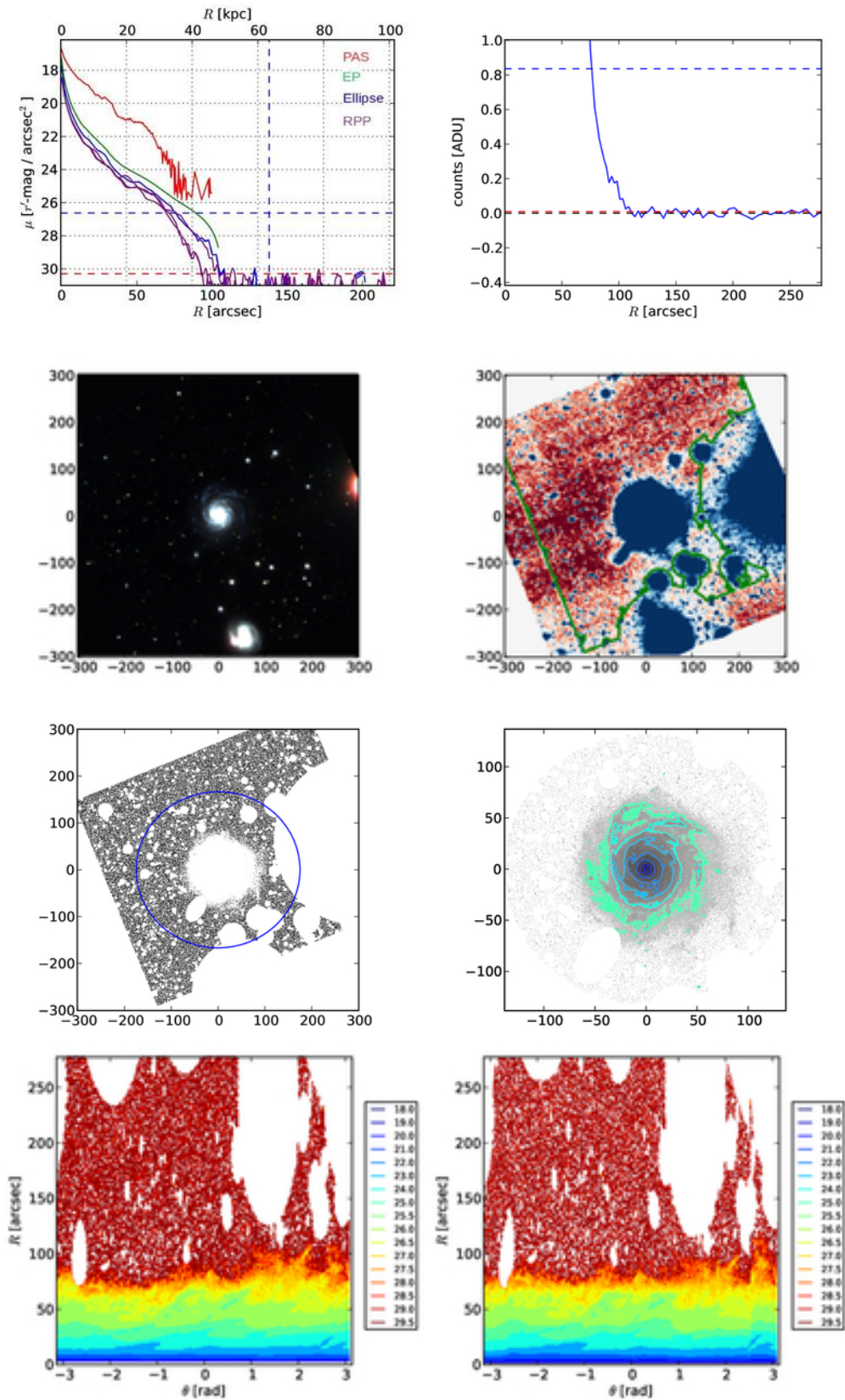


Figure A2. Results for IC 1516.

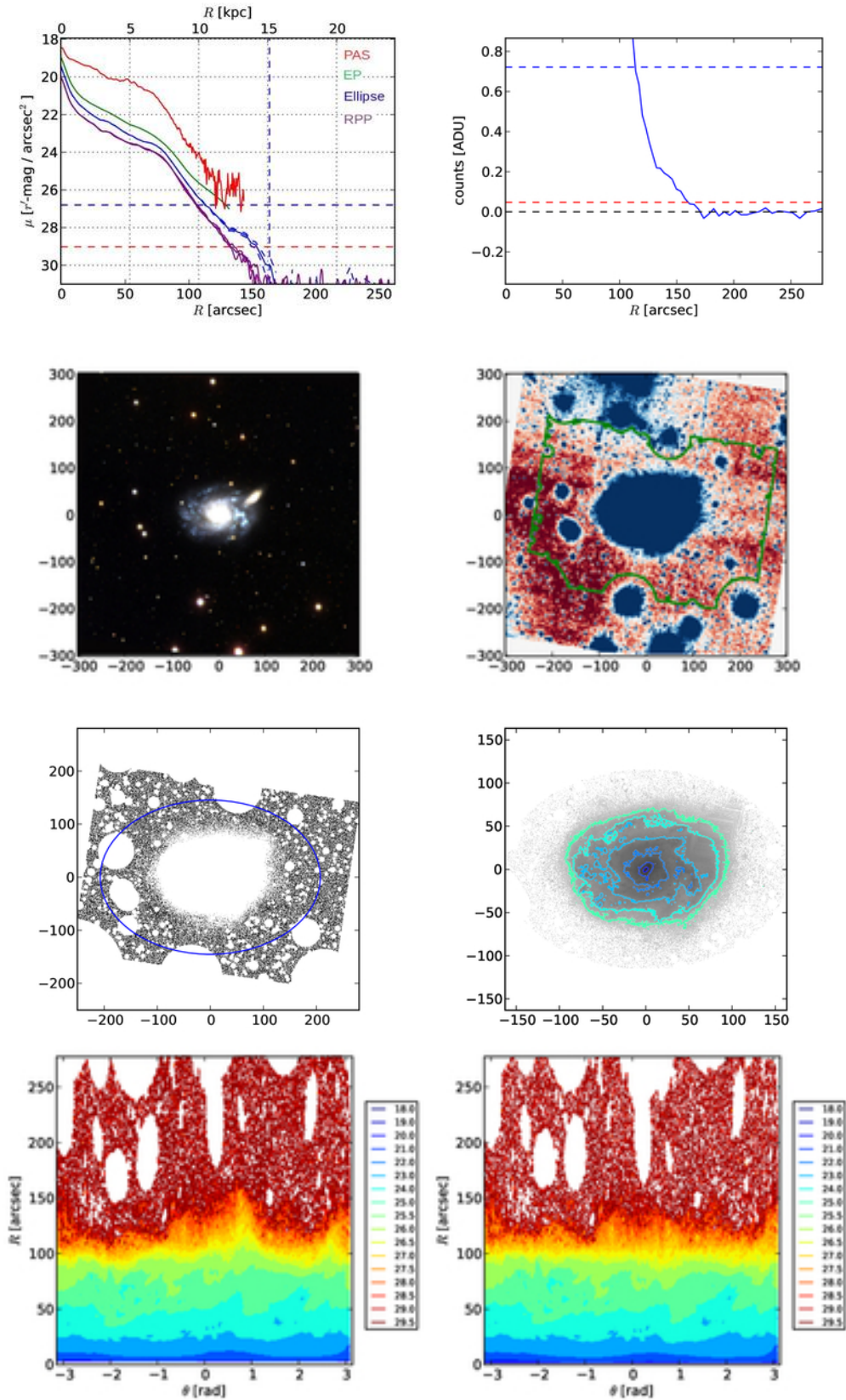


Figure A3. Results for NGC 450.

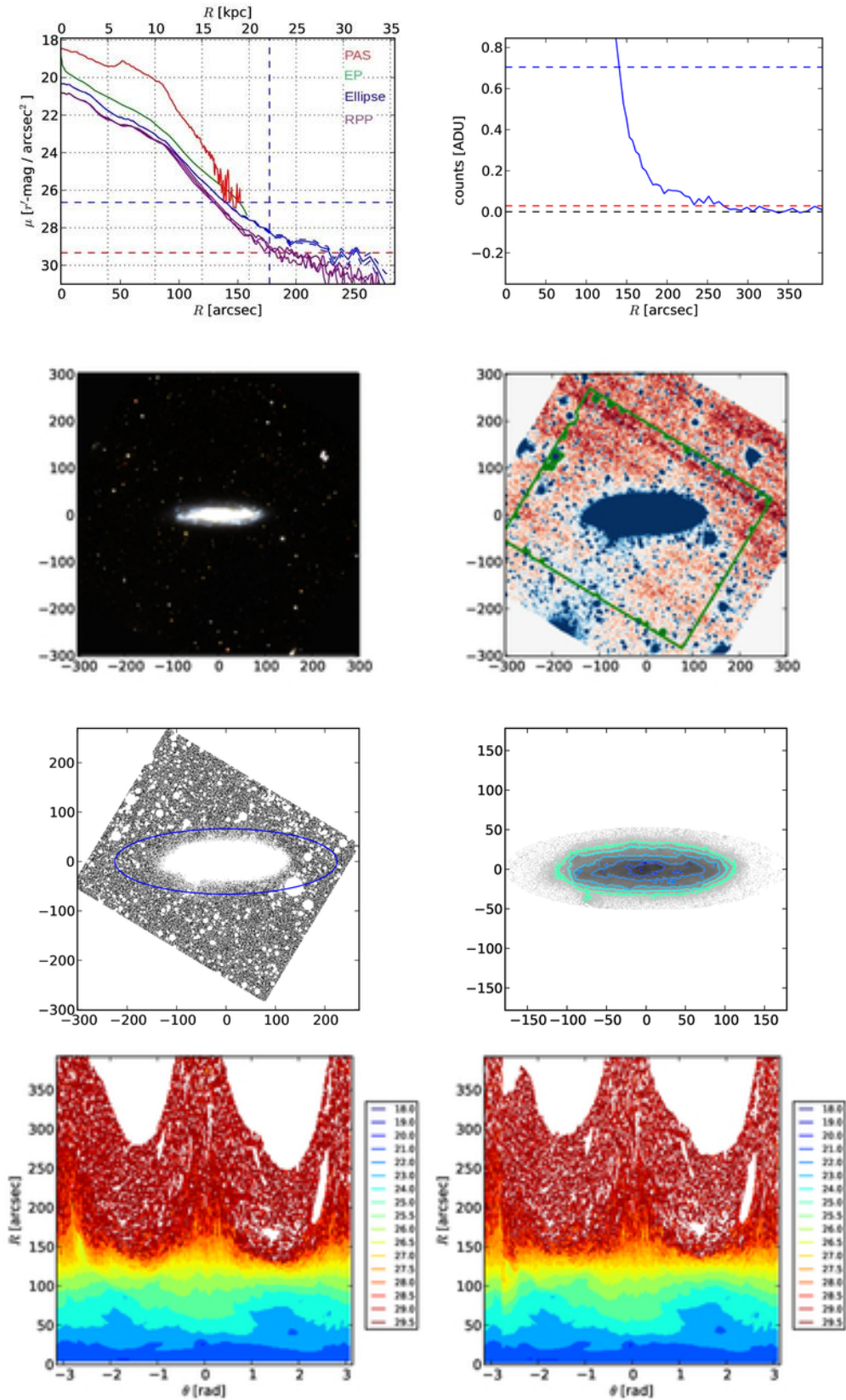


Figure A4. Results for NGC 493.

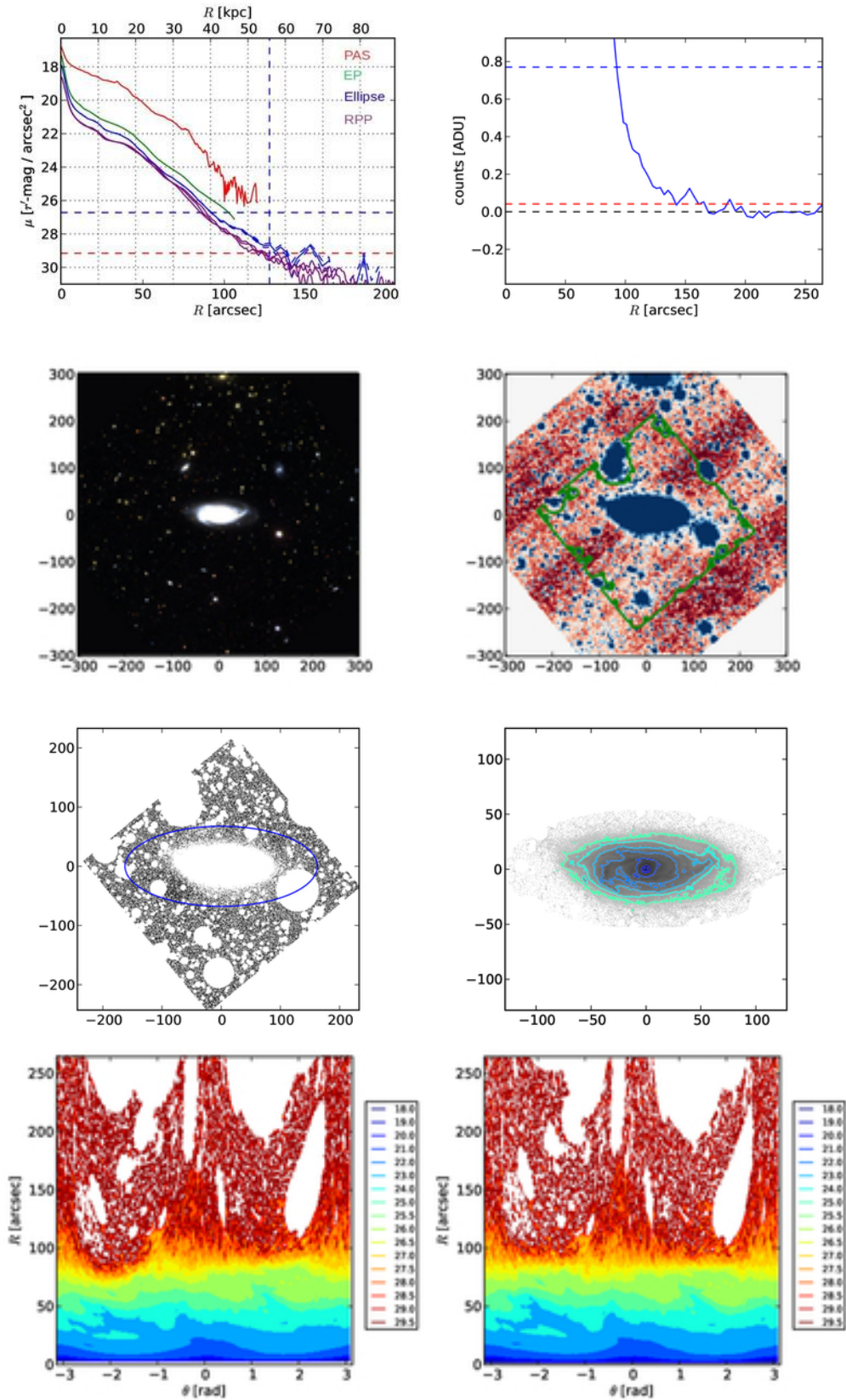


Figure A5. Results for NGC 497.

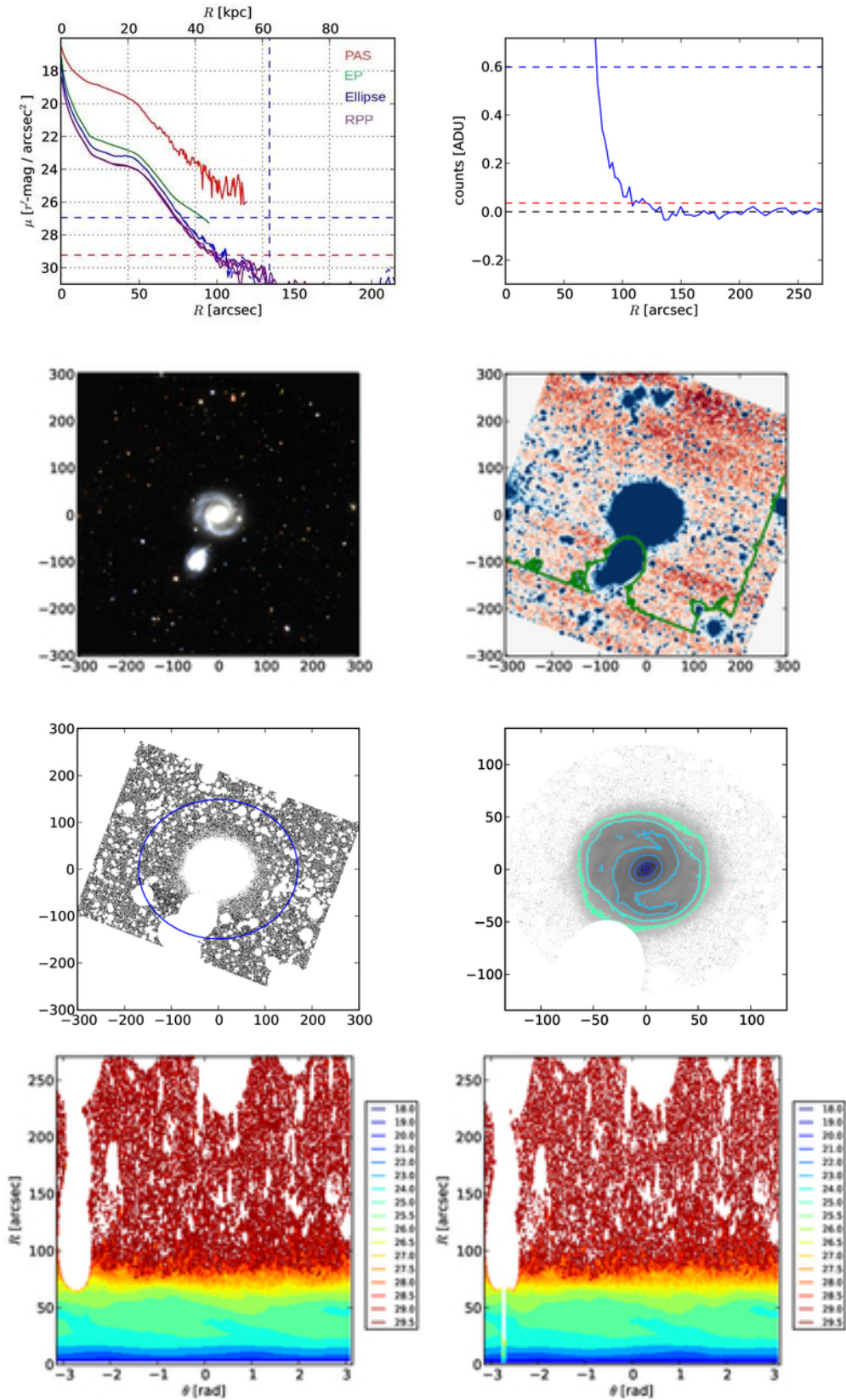


Figure A6. Results for NGC 799.

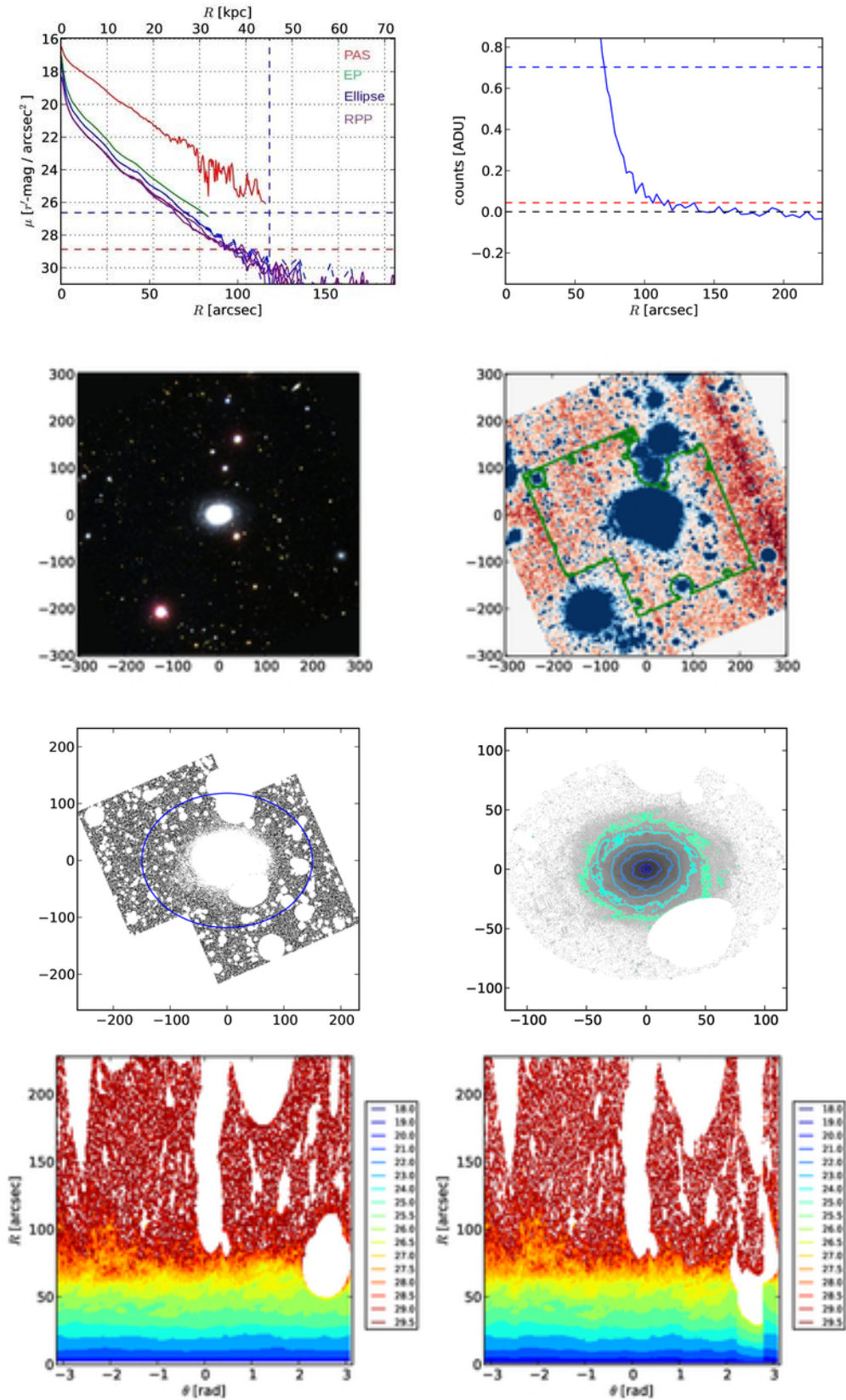


Figure A7. Results for NGC 856.

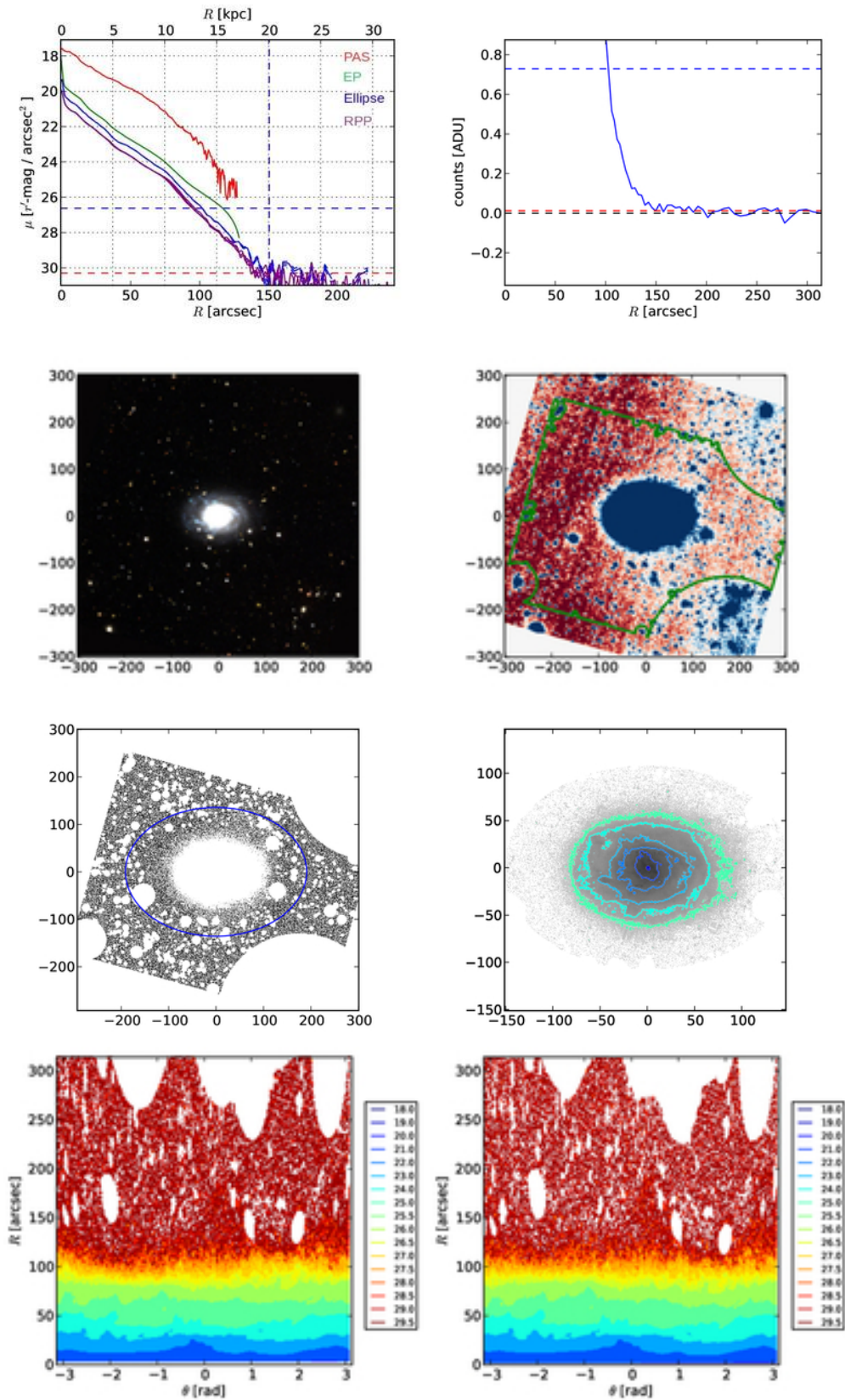


Figure A8. Results for NGC 941.

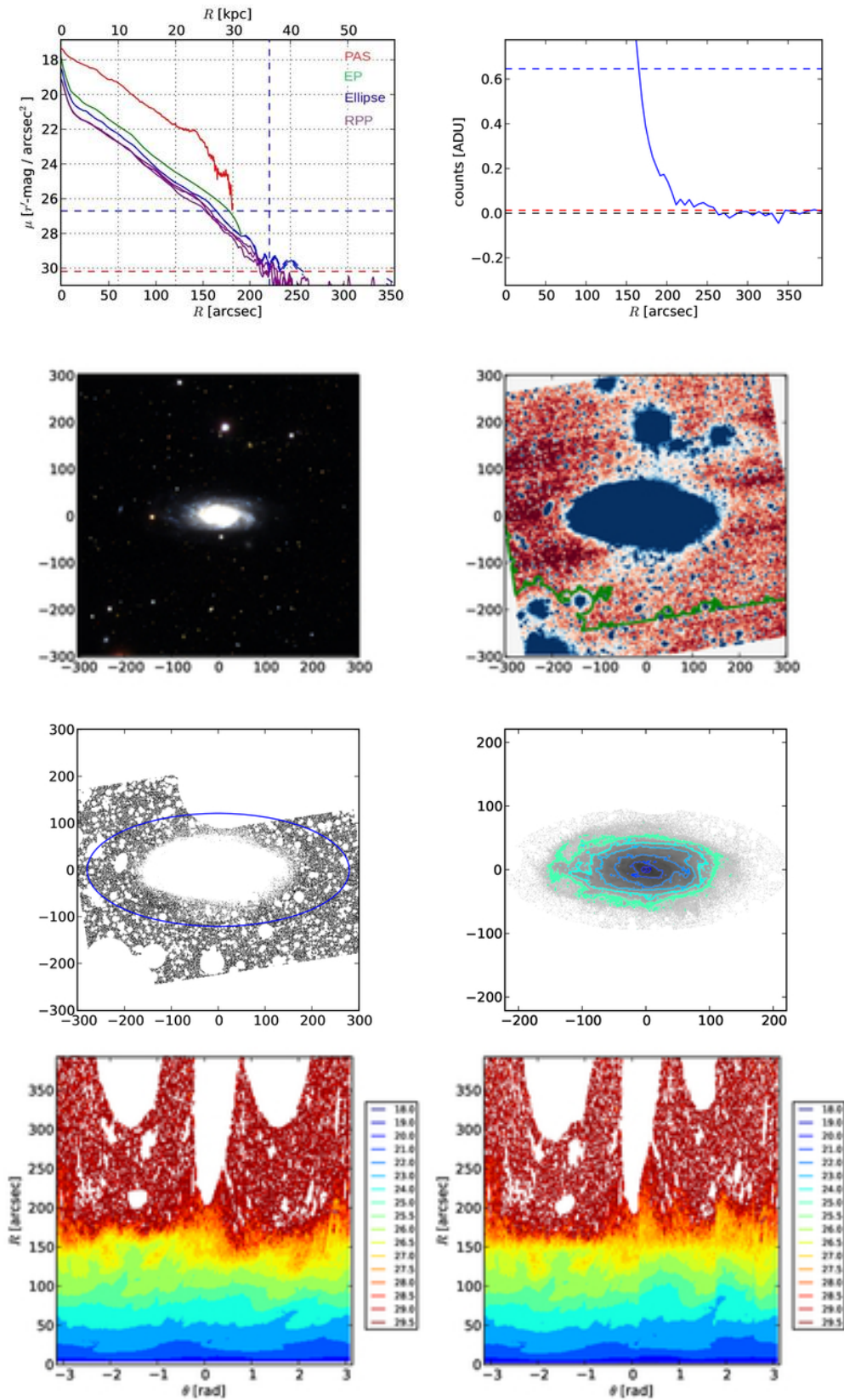


Figure A9. Results for NGC 1090.

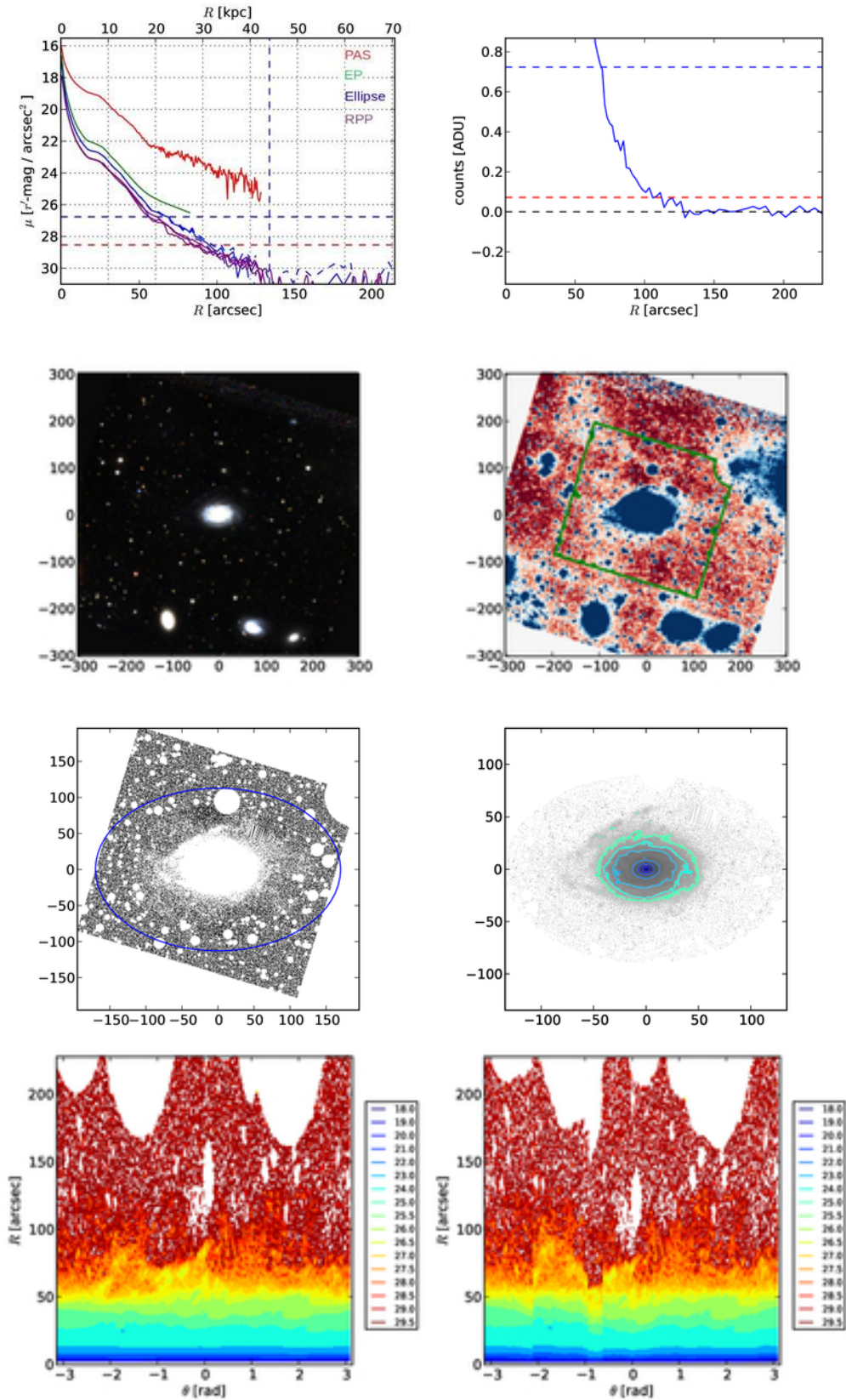


Figure A10. Results for NGC 7398.

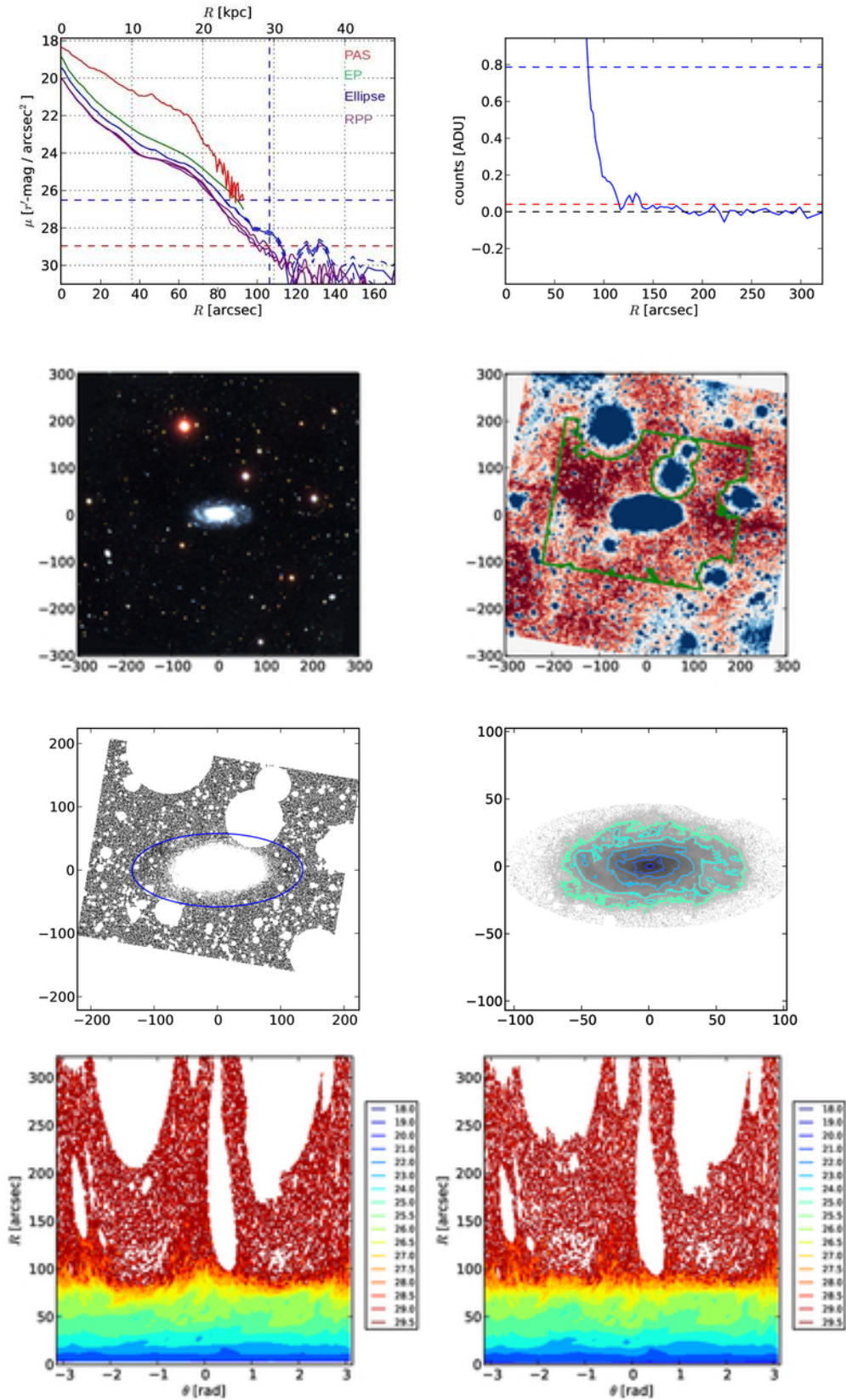


Figure A11. Results for UGC 139.

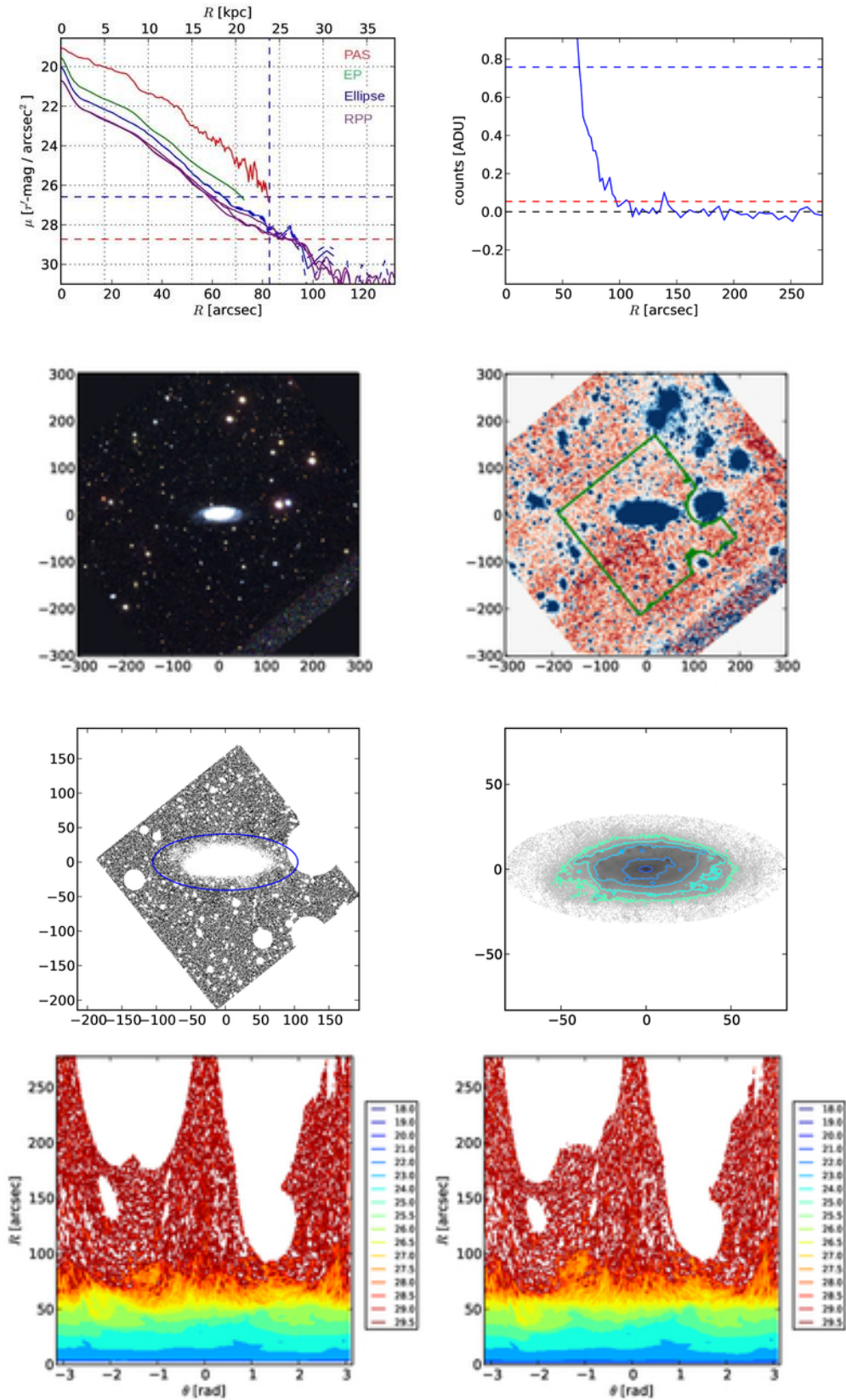


Figure A12. Results for UGC 272.

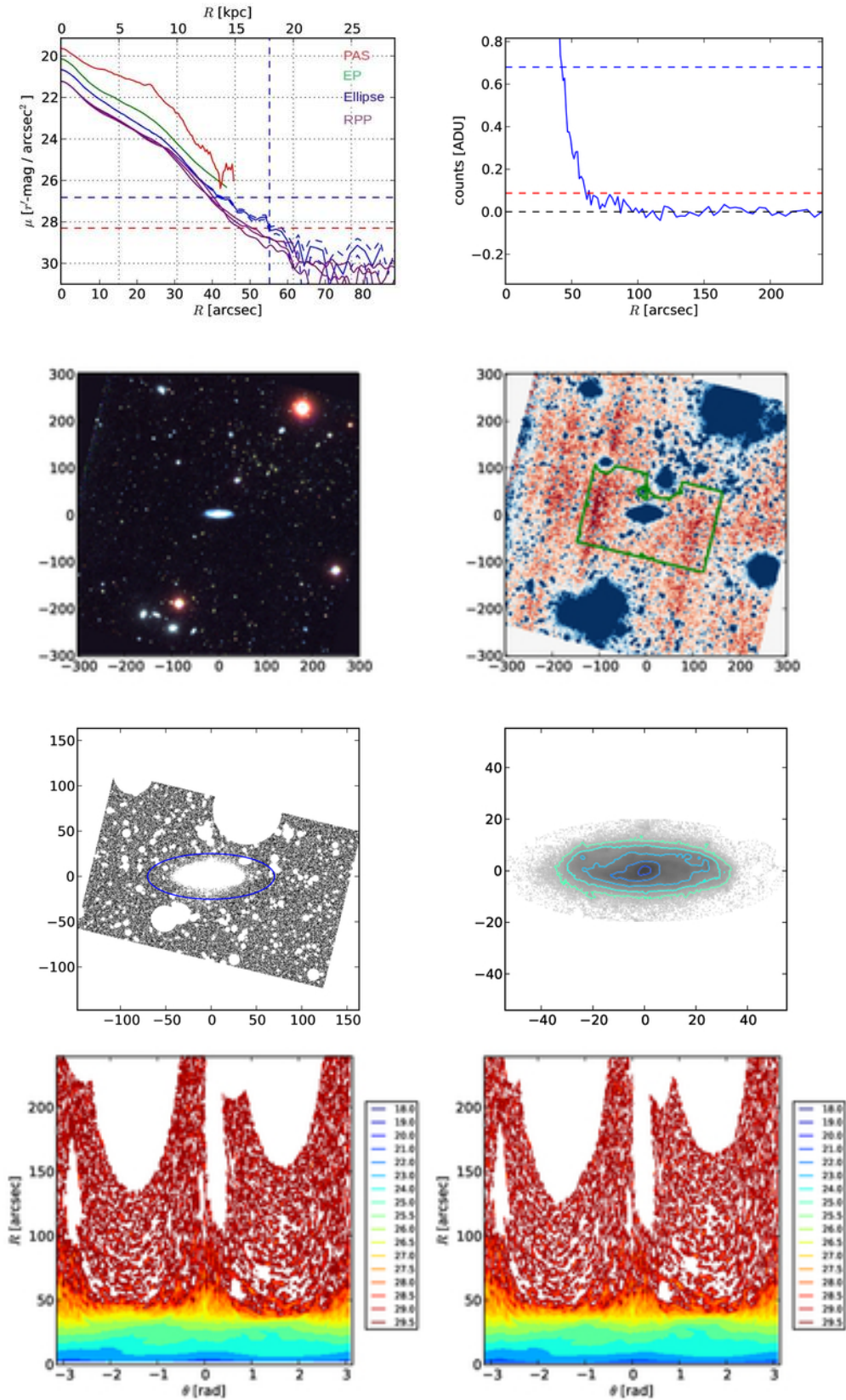


Figure A13. Results for UGC 651.

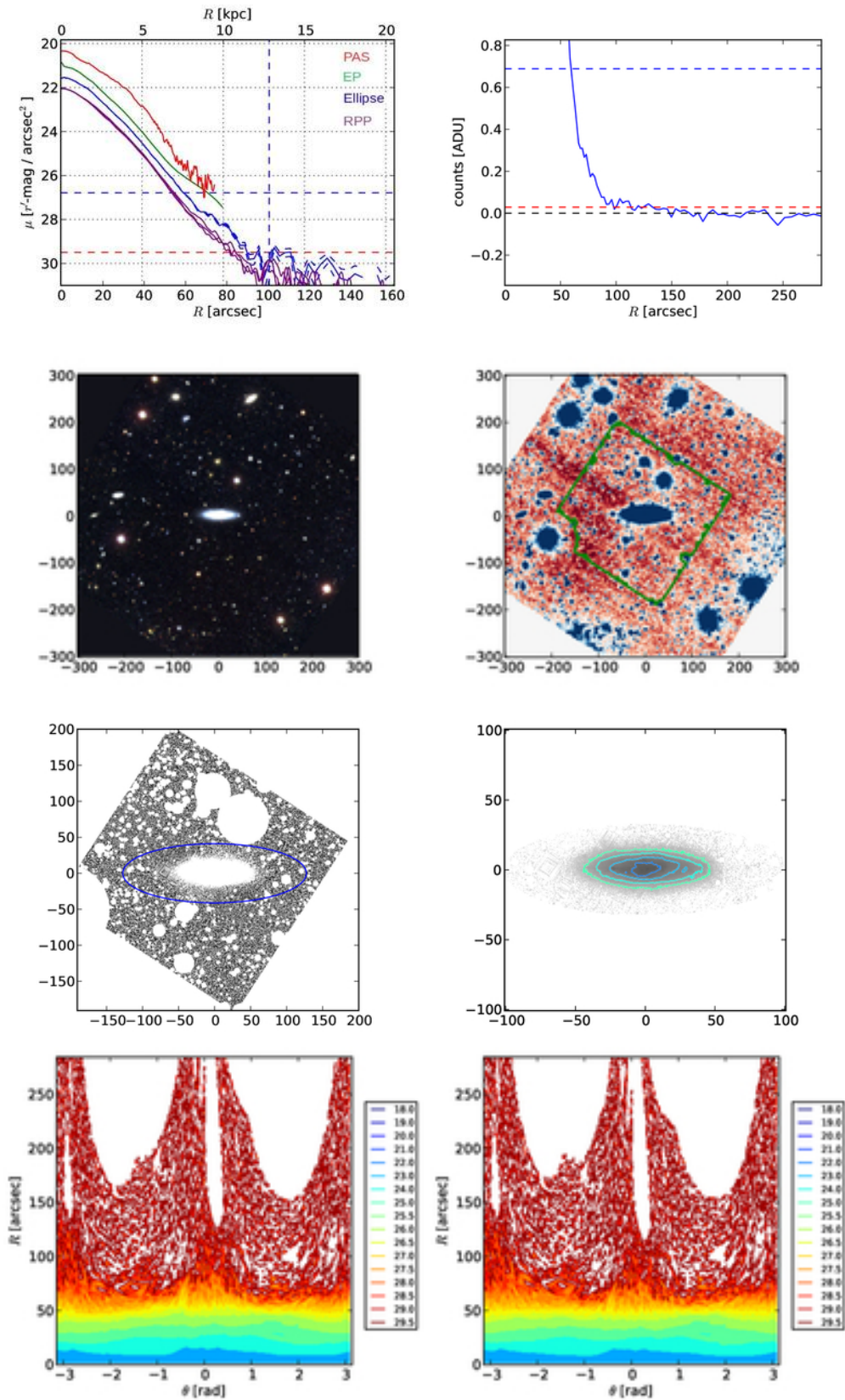


Figure A14. Results for UGC 866.

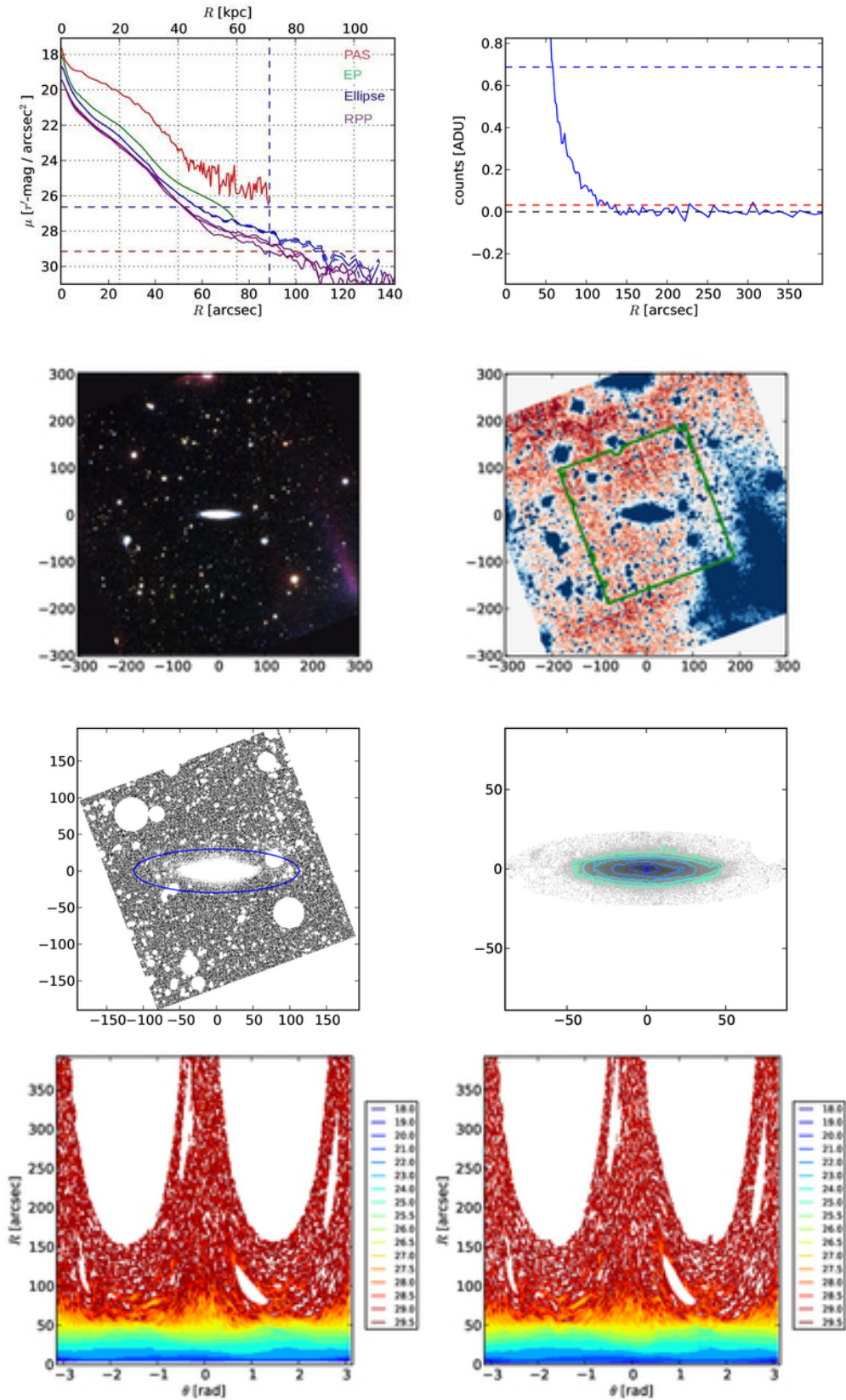


Figure A15. Results for UGC 1934.

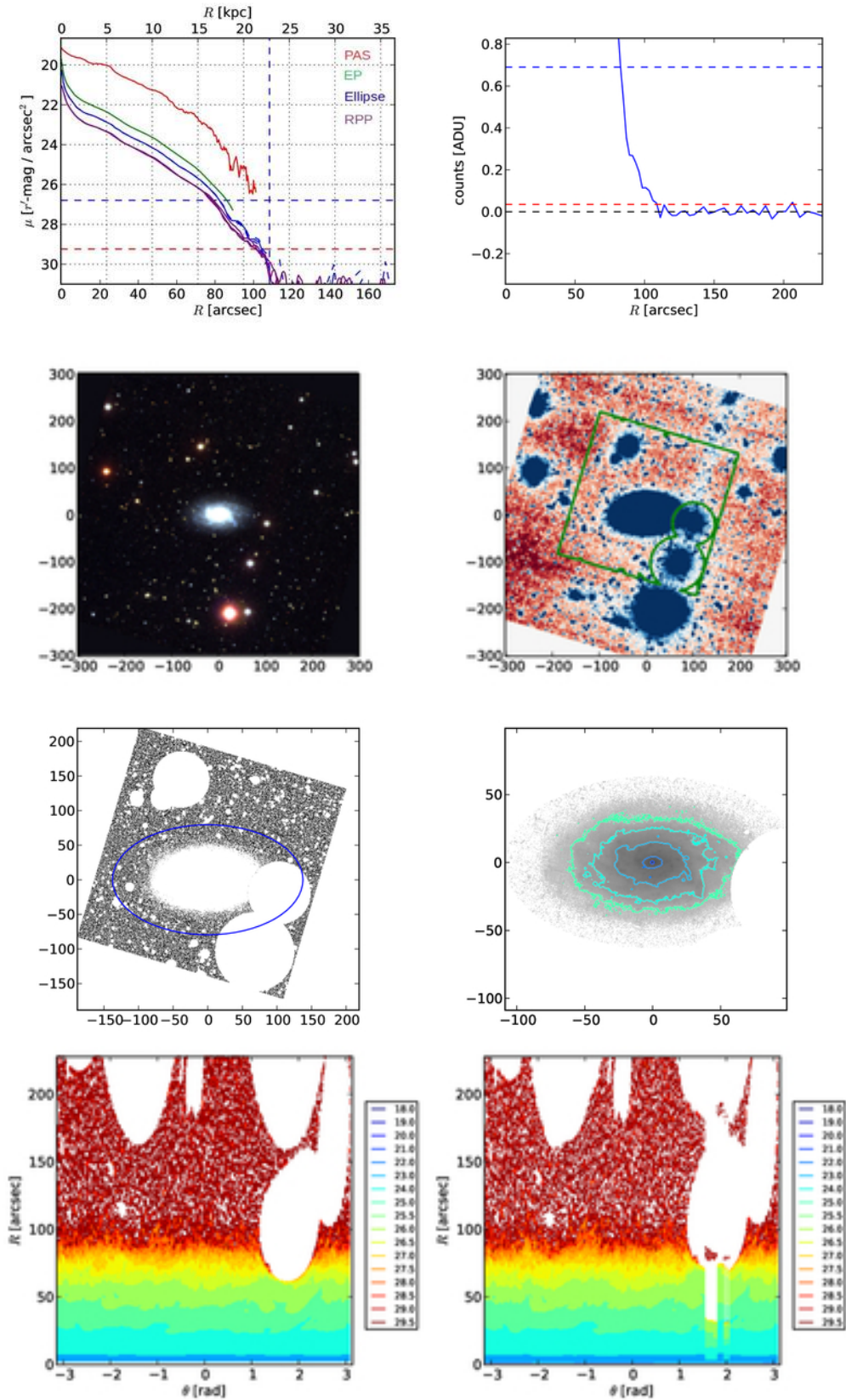


Figure A16. Results for UGC 2081.

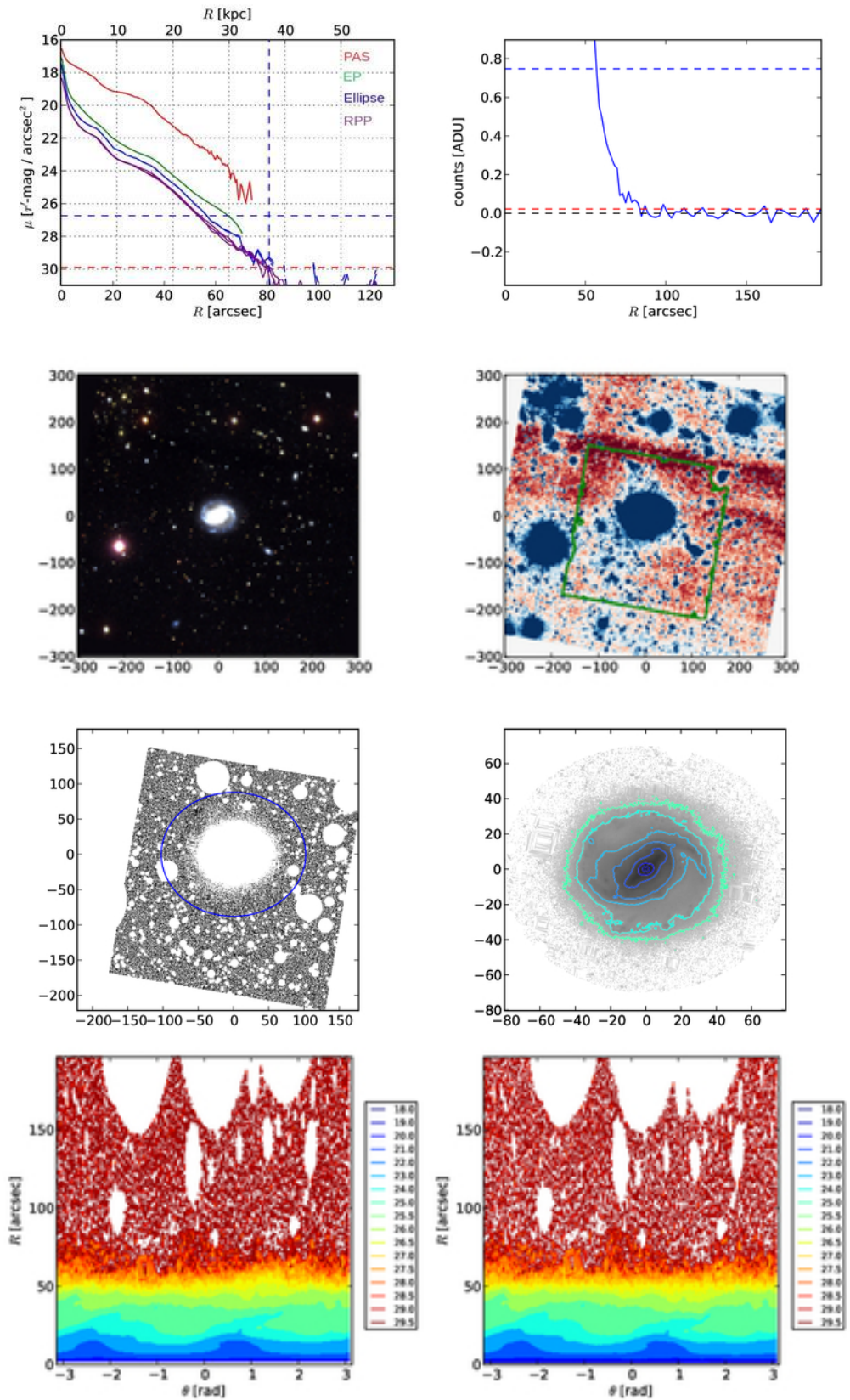


Figure A17. Results for UGC 2311.

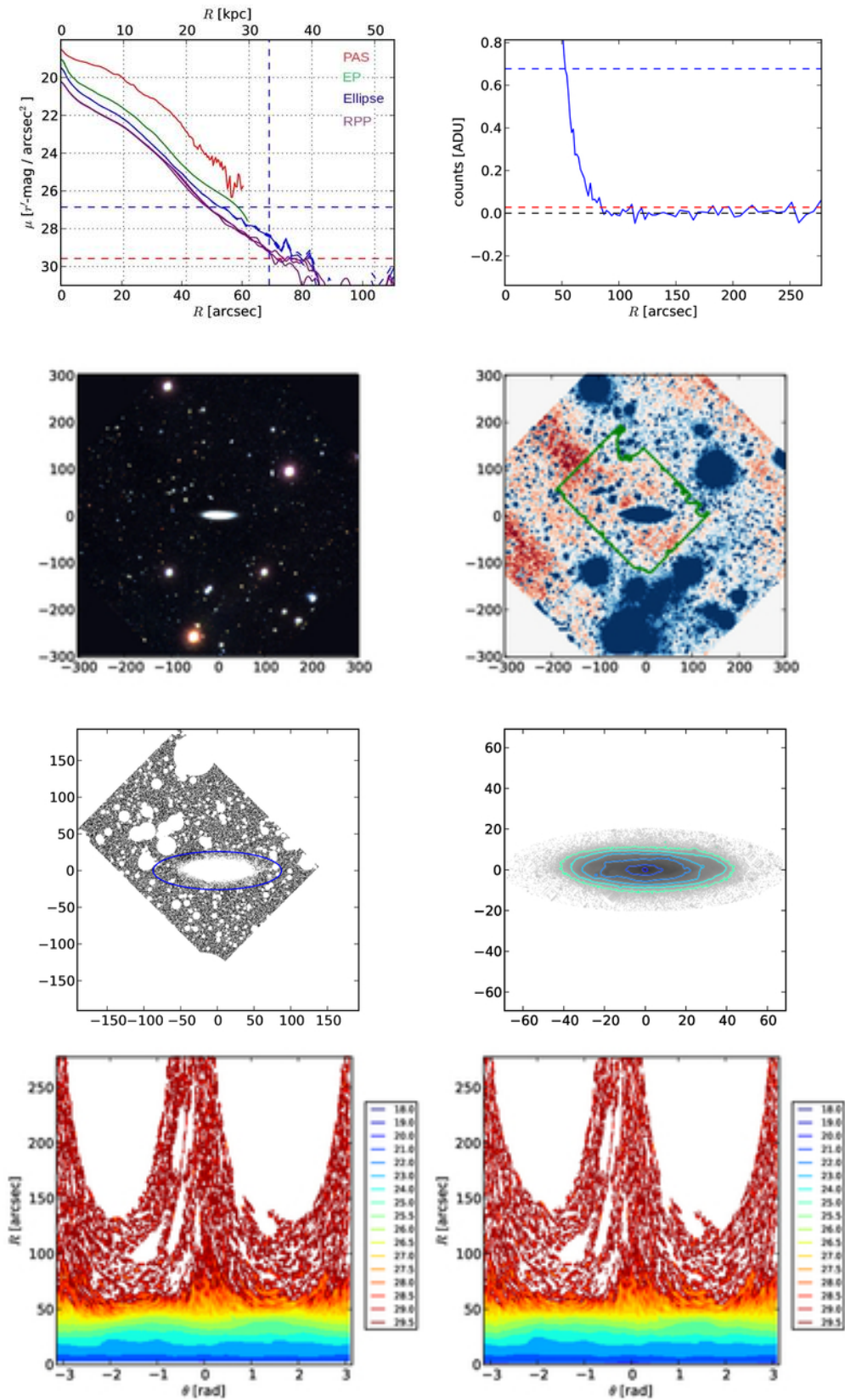


Figure A18. Results for UGC 2319.

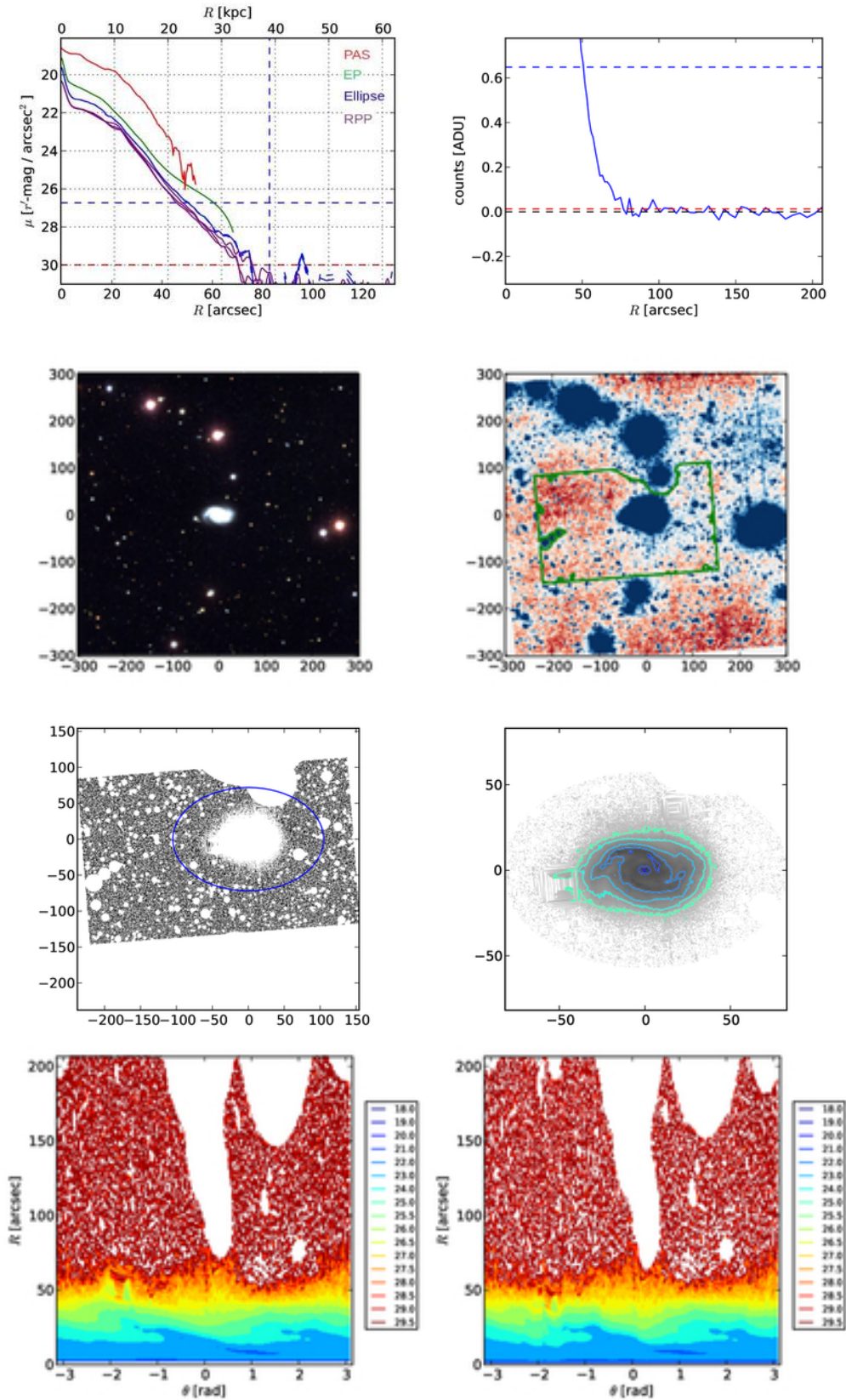


Figure A19. Results for UGC 2418.

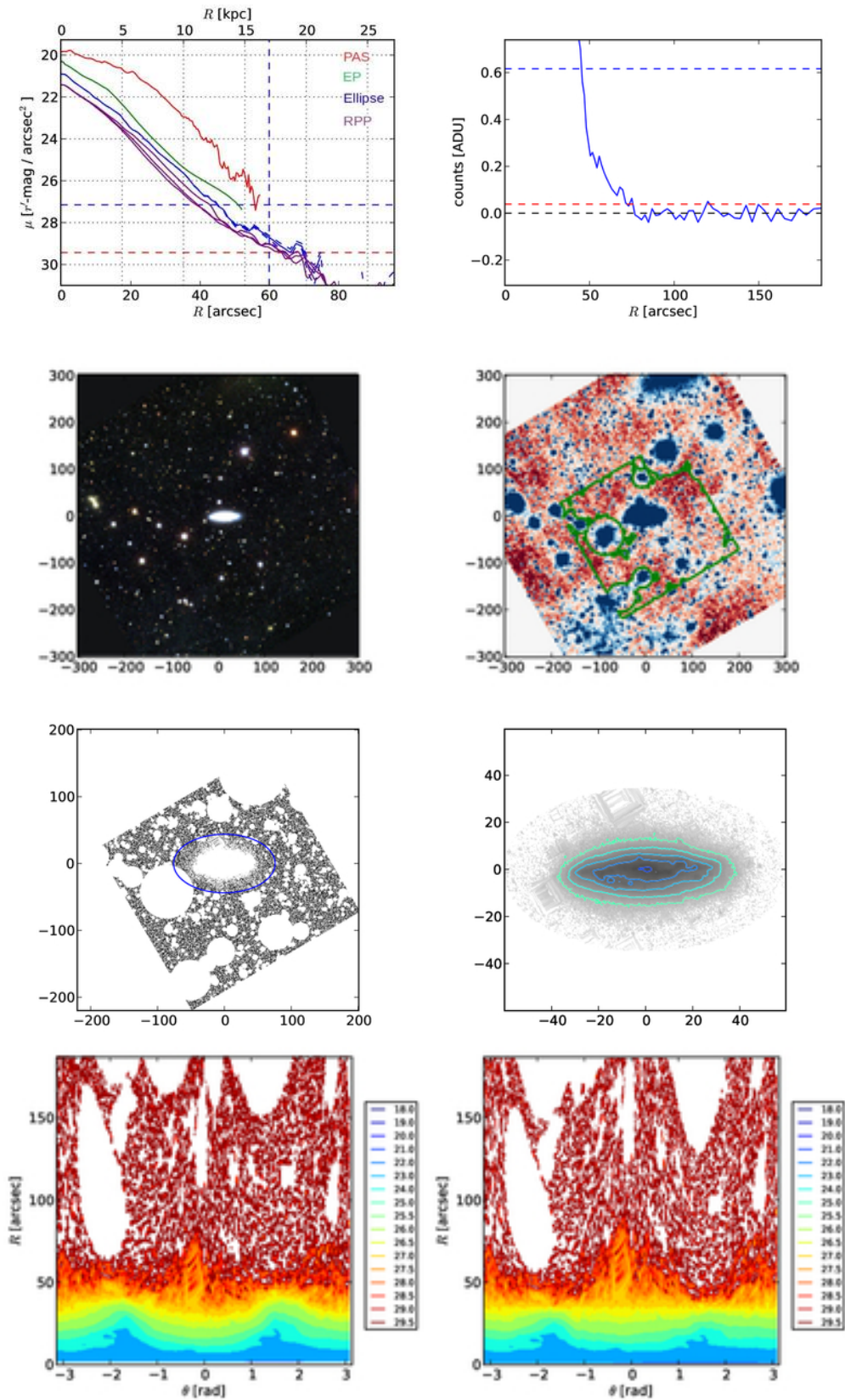


Figure A20. Results for UGC 12183.

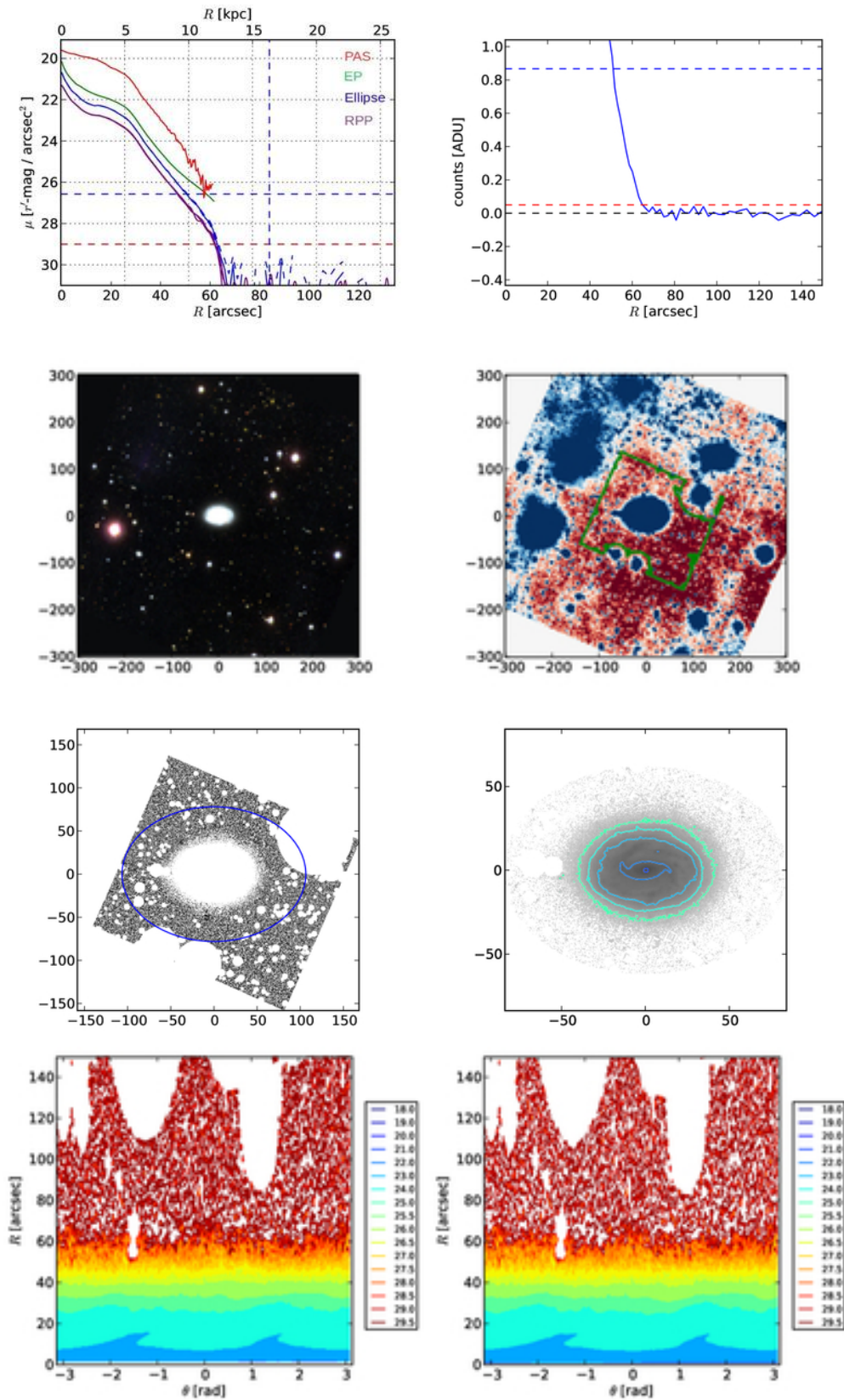


Figure A21. Results for UGC 12208.

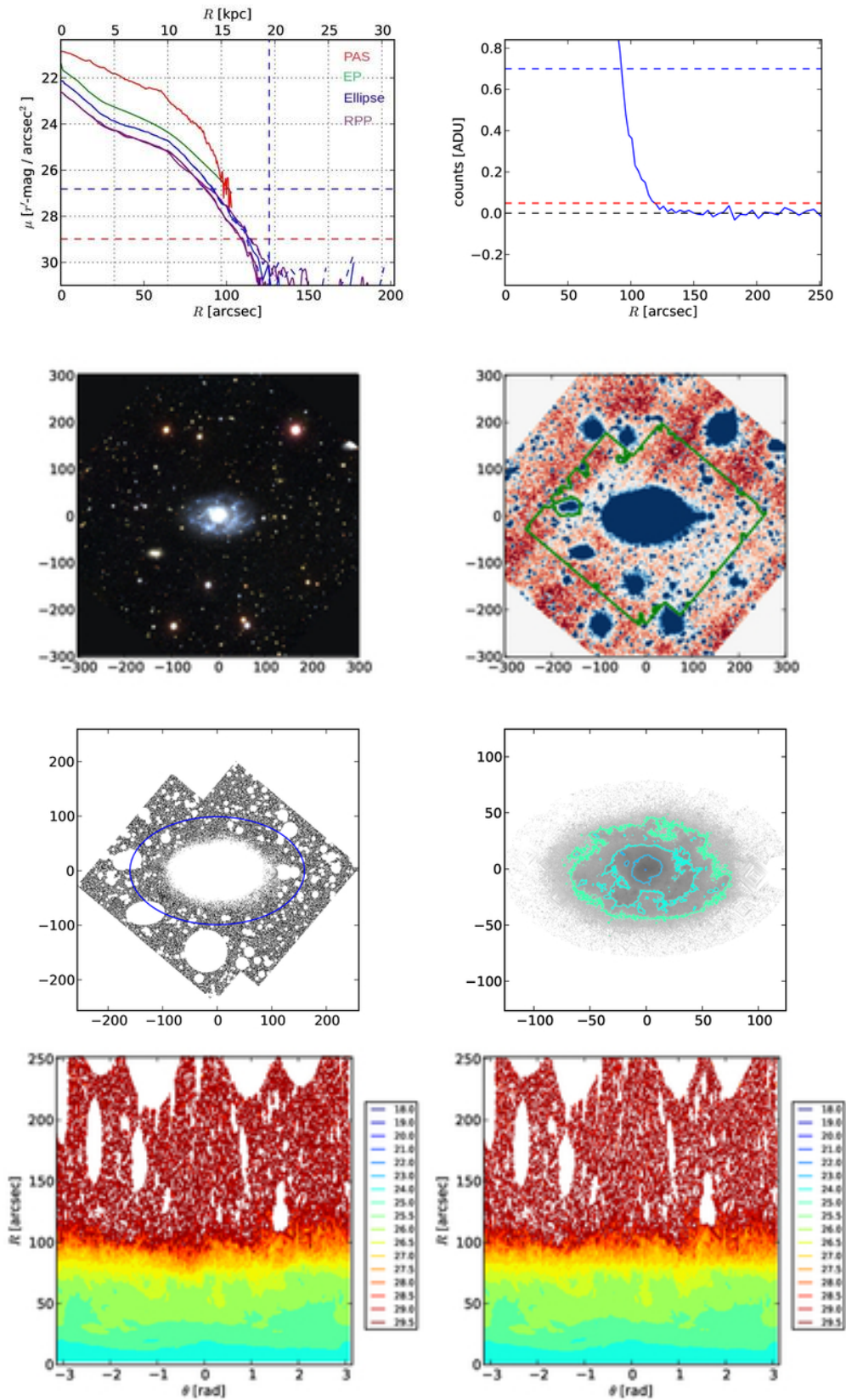


Figure A22. Results for UGC 12709.

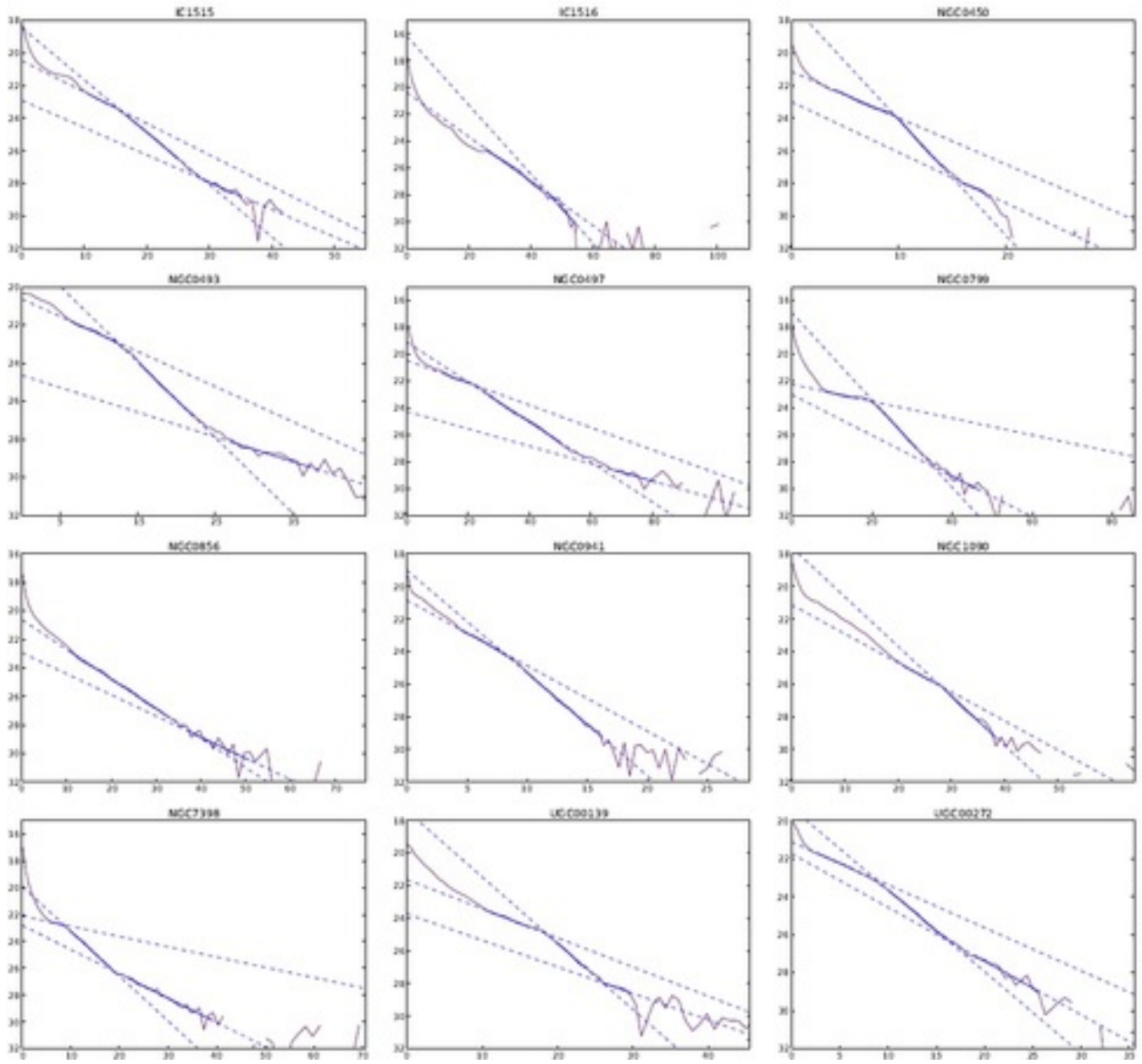


Figure A23. Results of the fits to the elliptical profiles. Magnitudes/arcsec² on the vertical axis, R in kpc on the horizontal axis.

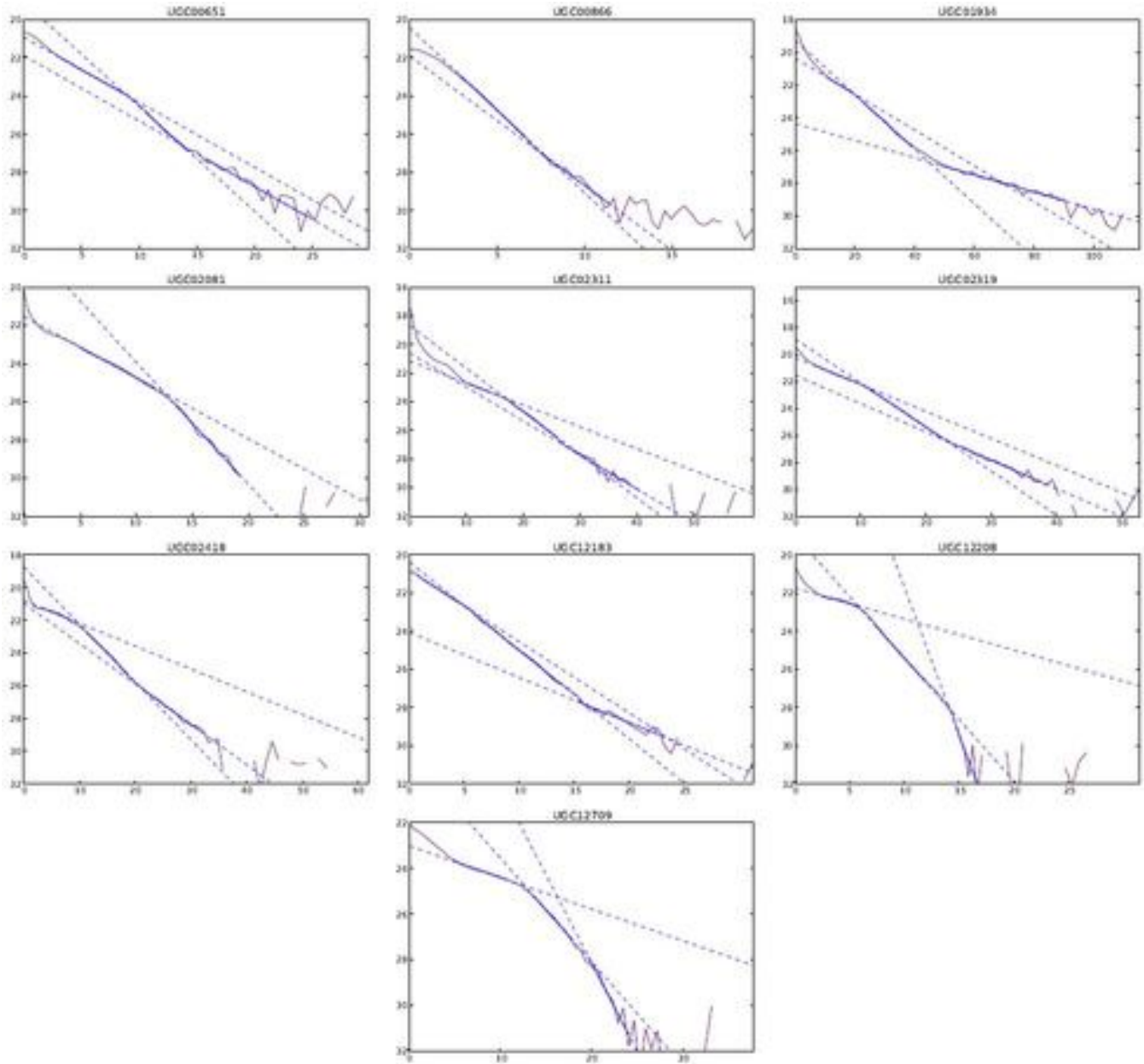


Figure A24. Results of the fits to the elliptical profiles. Magnitudes/arcsec² on the vertical axis, R in kpc on the horizontal axis.

This paper has been typeset from a \TeX / \LaTeX file prepared by the author.